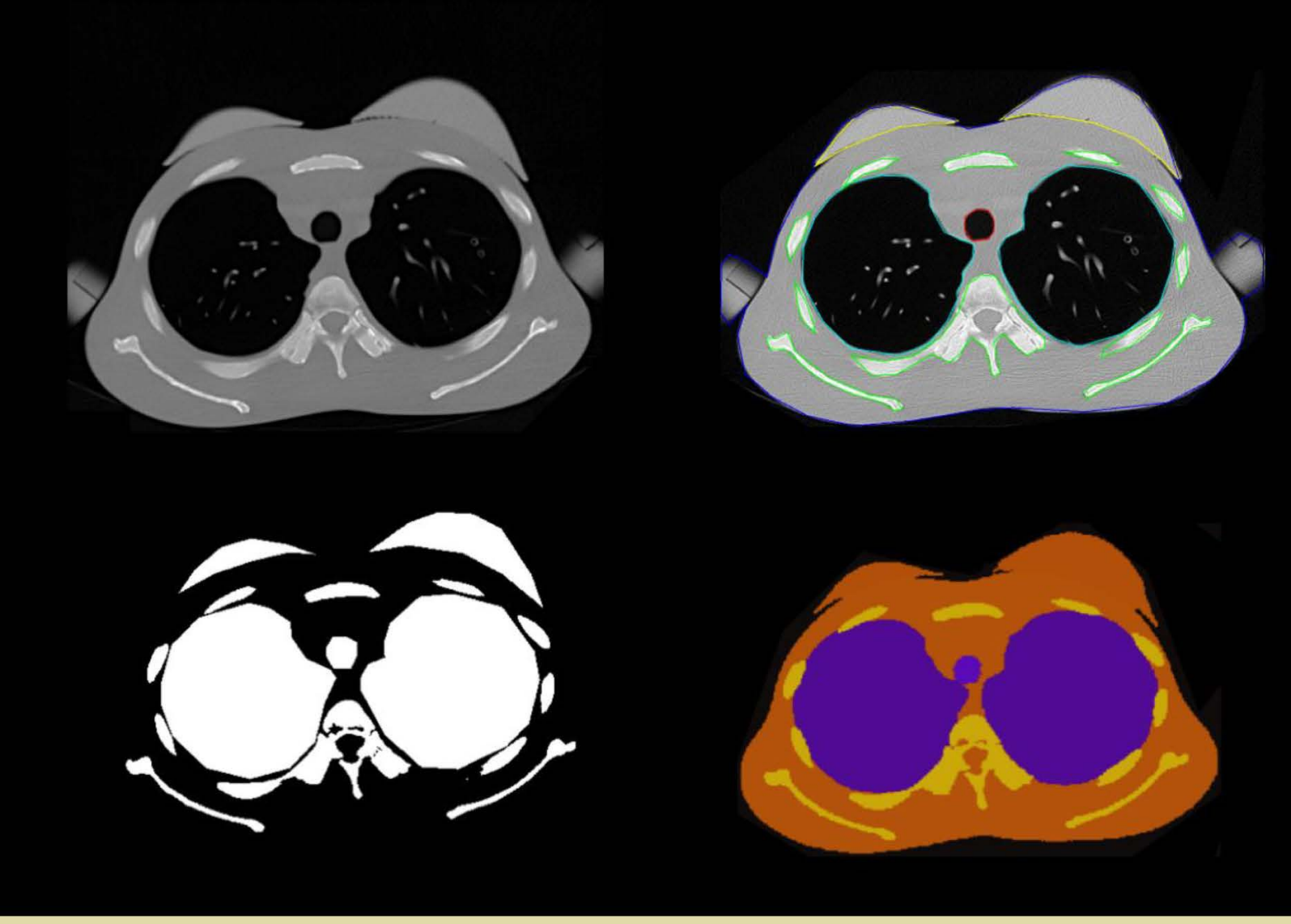

Ana Rita Coelho e Silva Honório Monteiro

IMAGE SEGMENTATION AND VOXELIZATION TECHNIQUES FOR DOSE ASSESSMENT IN X-RAY DIAGNOSTIC PROCEDURES

Dissertação submetida na Faculdade de Ciências e Tecnologias da Universidade de Coimbra
para obtenção do grau de Mestre em Engenharia Biomédica

Setembro 2017

· U C ·

UNIVERSIDADE DE COIMBRA

• U C •

FCTUC FACULDADE DE CIÊNCIAS
E TECNOLOGIA
UNIVERSIDADE DE COIMBRA

Ana Rita Coelho e Silva Honório Monteiro

Image Segmentation and Voxelization Techniques for Dose Assessment in X-Ray Diagnostic Procedures

Dissertion presented to the University of Coimbra
in order to complete the necessary requirements to
obtain the Master's degree in Biomedical Engineering.

Supervisors:
Ph.D. Salvatore di Maria (IST-CT2N)
Prof. Dr. Joana Santos Costa (ESTeSC)
Prof. Dr. Nuno Matela (FCUL)

Coimbra, 2017

This work was developped in collaboration with:

Escola Superior de Tecnologia de Saúde de Coimbra

Instituto de Biofísica e Engenharia Biomédica

Campus Tecnológico e Nuclear do Instituto Superior Técnico

Acknowledgments

Com o culminar de uma etapa, vêm à memória todos os momentos e amizades criadas ao longo deste percurso e não posso deixar de me sentir grata por tudo o que tenho recebido.

Em primeiro lugar, deixar o meu maior agradecimento ao Prof. Salvatore di Maria, à Prof. Joana Santos e ao Prof. Nuno Matela, que me acompanharam ao longo deste ano e que sempre se mostraram disponíveis para me orientarem, apoiarem e responderem a todas as minhas questões.

Ao Prof. Alexandre Lindote, agradeço a disponibilidade, ajuda e interesse demonstrado por este projecto.

Deixar um agradecimento ao Serviço de Imagem Médica do CHUC, em particular ao seu director Professor Doutor Caseiro Alves e à Técnica Coordenadora Dra. Alda Pinto, pela disponibilidade na acquisição das imagens.

Não posso deixar de agradecer aos meus colegas do IBEB, em especial à Raquel, pela companhia nas horas de trabalho e de almoço e por me terem ajudado a ambientar numa nova cidade. De igual modo, agradecer aos meus colegas do CTN, em especial à Débora e ao Jorge, por todas as indicações e ensinamentos relativamente ao código PenEasy.

À Alexandra, à Maria, à Maria Inês, à Mariana, à Rita, à Sara e à Verónica, as grandes amigas que tive a sorte de conhecer, que sempre me apoiaram e motivaram ao longo destes de 5 anos, um enorme obrigada do fundo do meu coração! Levo-vos comigo para a vida!

À Benedita e à Isabelinha, os acasos que viram escolhas, obrigada pela amizade, pelos conselhos e exemplos. Aos amigos do Trianon, aos amiguinhos, às mosqueteiras, à minha família internacional, à Sara Raquel, ao Rebelo e aos outros grandes amigos que tenho a sorte de serem uma constante na minha vida, me incentivarem sempre a ir mais longe e fazerem cada momento valer a pena.

Por último, o meu maior agradecimento aos que tornam tudo possível. À minha mãe que desde que eu me lembro me faz acreditar que sou capaz. Ao meu pai, aos meus irmãos, e aos meus avós por me mostrarem como ser feliz, me ensinarem muito do que sei hoje e, principalmente, por me ajudarem a sonhar e apoiarem em cada escolha. Obrigada por serem a razão de querer sempre voltar a casa!

Resumo

Ao longo dos últimos 50 anos, devido aos riscos de exposição à radiação e, consequentemente, à impraticabilidade da expor pacientes a radiação para medidas dosimétricas, foram introduzidos fantomas computacionais para avaliar a dose de radiação. Os fantomas computacionais de voxel modelam a anatomia humana e são utilizados no campo da proteção contra a radiação, da imagem médica e radioterapia uma vez que permitem a avaliação da doses nos órgãos com elevado grau de precisão. Embora se tenha vindo a constatar um recente aumento no número de fantomas computacionais disponíveis, o objectivo máximo da dosimetria da radiação, passa por obter um modelo computacional para cada paciente envolvido em processos de radiação. Partindo deste princípio, o objetivo deste estudo é tentar melhor a implementação um fantoma de voxel computacional a partir de imagens médicas de um fantoma físico para avaliar, de forma precisa, a dose depositada nos órgãos devido à utilização de raios-X para diagnóstico médico.

Foi utilizado um scanner de tomografia computadorizada (TC) Siemens SOMATOM Definition 64, em operação no Hospital Pediátrico do Centro Hospitalar da Universidade de Coimbra, para adquirir imagens de TC ao tórax de um fantoma antropomórfico, o Kyoto PBU-60. Diferentes técnicas de segmentação, como métodos de *thersholding* e algoritmos de *region growing*, foram aplicadas às imagens médicas adquiridas, com o objectivo de extrair os diferentes órgãos radiossensíveis. Para definir o fantoma de voxel, os números de TC de cada órgão foram convertidos em valores de densidade através do uso de uma curva de calibração. Os valores de densidade dos órgãos do fantoma foram comparados com valores de referência estabelecidos pela ICRP, revelando uma comparação bem sucedida em 9 dos 11 órgãos ou tecidos segmentados.

A segunda parte deste trabalho consistiu no uso de métodos de Monte Carlo (MC) (código PENELOPE), para desenvolver e validar o modelo de aquisição (equipamento TC e fantoma) de modo a avaliar doses nos órgãos e estudar a otimização da qualidade de imagem para diferentes espessuras de calcificações. Foi obtida diferença relativa de 13.813 % entre resultados experimentais e simulados para $CTDI_{100}$ o que,

considerando todas as incertezas envolvidas, permite a aprovação do uso do fantoma voxel para avaliação de dose nos órgãos.

Finalmente, de modo a mostrar outra aplicação dos fantomas computacionais, foi realizada uma análise da relação sinal-ruído diferencial (SDNR) para diferentes tamanhos de calcificações. Esta análise, demonstrou que 60 keV é o valor de energia de raios-X adequada para espessuras de 0.7 cm.

Palavras-chave: Fantomas de Voxel; Dose nos órgãos; Diagnóstico de raio-X; Segmentação; Simulações de Monte Carlo; Qualidade de imagem

Abstract

Over the last 50 years, due to the risks of radiation exposure and, consequently, to the impracticality to expose humans to radiation for dosimetric measurements, computational phantoms have been introduced for radiation dose assessment. Computational voxel phantoms are models of the human anatomy used in the field of radiation protection, medical imaging and radiotherapy that enables evaluation of organ doses with a high degree of precision. Although there was a recently huge increase in the number of computational phantoms available, the gold standard of radiation dosimetry, would be to obtain a computational model for each patient involved in radiation processes. Starting from this principle, the aim of this study was to try to improve the implementation of a computational voxel phantom starting by a physical one for precise organs dose assessment in the field of X-ray diagnostic.

A Siemens SOMATOM Definition 64 slice CT scanner at operation in the Paediatric Department of Coimbra Hospital and University Centre was used to perform chest CT examinations with an anthropomorphic phantom named Kyoto PBU-60. Segmentation techniques, as thresholding methods and region growing algorithms were applied to the medical images acquired in order to extract radiosensitive organs. To define the voxel phantom, the CT numbers of each organ were converted to density values using a calibration curve. A successful comparison of the densities of the phantom organs against reference values established by ICRP was achieved for 9 out of the 11 organs and tissues segmented.

The second part of the work consisted in using Monte Carlo (MC) methods (PENELOPE code), in order to develop and validate an acquisition setup model (phantom and CT equipment) to study organ doses and image quality optimization for different calcifications thickness. A relative difference of 13.813 % between experimental and simulated results for $CTDI_{100}$ was accomplished, which, considering all the uncertainties involved, can be considered satisfactory for using the voxel phantom in organs dose assessment tasks.

Finally, in order to show another application of computational phantoms, an analysis of signal-to-difference noise ratio for different calcifications sizes was per-

formed. This analysis, revealed an optimal X-ray energy of 60 keV for a 0.7 cm thickness.

Keywords: Voxel phantoms; Organ doses; X-Ray diagnostic; Segmentation; Monte Carlo simulations; Image Quality

List of Figures

List of Tables

Acronyms

AAPM American Association of Physicists in Medicine
ACR The American College of Radiologists
AHARA *as high as reasonably achievable*
ALARA *as low as reasonably achievable*
ANN Artificial Neural Network
AP Anteroposterior Dimension
BREP Boundary Representation
CARE Combined Applications to Reduce Exposure
CF Conversion Factor
CNR Contrast-to-noise Ratio
CSG Constructive Solid Geometry
CST Central Slice Theorem
CT Computed Tomography
CTDI Computed Tomography Dose Index
$CTDI_{vol}$ Pitch Corrected CT Dose Index
$CTDI_w$ Weighted Computed Tomography Dose Index
DICOM Digital Imaging and Communications in Medicine
DLP Dose Length Product
DRL Diagnostic Reference Levels
EURATOM European Atomic Energy Community
EUROSTAT Statistical Office of the European Communities
FAST Fully Assisting Scanner Technologies
FBP Filtered Backprojection
FDA Food and Drug Administration
FPR False Positive Rate
FT Fourier Transform
HRCT High Resolution Computed Tomography

HU Hounsfield Unit

IC Ionisation Chamber

ICRP International Commission on Radiological Protection

ICRU International Commission on Radiation Units and Measurements

IEC International Electrotechnical Commission

LAT Lateral Dimension

Kerma Kinetic Energy Released in the Material (or per unit Mass)

MC Monte Carlo

MIRD Medical Internal Radiation Dosimetry

MRI Magnetic Resonance Imaging

NURBS Non-Uniform Rational Basis Spline

ORNL Oak Ridge National Laboratory

OSLD Optically Stimulated Luminescent Dosimeter

PENELOPE PENtration Energy Loss Of Positrons and Electrons

PMMA Polymethyl Methacrylate Phantoms

RP Radiation Protection

ROI Region of Interest

SDNR Difference Signal-to-Noise Ratio

SNR Signal-to-Noise Ratio

SSDE Size-Specific Dose Estimates

TLD Thermoluminescent Dosimeter

UNSCEAR United Nations Scientific Committee for the Effects of Atomic Radiation

WL Window Level

WD Window Width

Indice

Chapter 1

Introduction

1.1 Context, Motivation and Goals

Phantoms are physical or virtual representations of the human body that have been used in medical physics and health physics. When the risks of exposure to radiation were studied, health professionals felt the necessity to simulate patients to make dosimetric measurements and to test limitations of imaging systems [1].

In the last 50 years, phantoms have become popular and are used in several medical physics applications. Therefore, the phantom purpose influences the physical design of the phantom such as size, shape and composition, and also, determines if the phantom contains places to insert dosimeters. Despite the materials that compose a phantom intend to simulate human tissues, the properties of the materials depend on the energy of the radiation energy incident. As a result, materials of a phantom developed to evaluate the organ doses during radiation therapy are completely different from the materials of a phantom used to test imaging limits of a radiographic system [1].

Since in the diagnostic imaging field, the imaging process involves the exposure of patients to X-rays and gamma-rays, with a high penetration depth in human tissues, and with a probability to induce cancer, health professionals have been using phantoms in order to understand how radiation interacts with the human body and to ensure safety of workers and members of the public [2].

The effects of exposure to high-dose radiation at cellular level can be categorised into 'deterministic' and 'stochastic'. The 'stochastic' effects can arise from damage

to a single cell, and its probability of occurrence increases with increasing of radiation dose. 'Stochastic' effects are related to the potential risk of induce malignancy [3]. On the other hand, 'deterministic' effects, occur normally for higher doses, i.e., if a dose threshold is exceeded the effect severity increases. Erythema, cell squamation and eye cataracts are examples of this effects [3].

With the aim of minimising radiation exposure to patients or to health professionals and reducing radiation effects, international organisations, as International Commission on Radiological Protection (ICRP), European Atomic Energy Community (EURATOM) have stated ALARA principle, 'as low as reasonably achievable', and several guidelines and recommendations for radiation procedures [4]. According to Council Directive 96/29 EURATOM, ALARA principle is based on three concepts: time, distance and shielding. In other words, dose can be reduced by reducing the distance between the source and the patient, by decreasing the time of exposure and increasing radioprotection. Diagnostic reference levels (DRL), are also important in radioprotection since they define the levels of exposure for typical examinations, performed in standard patients, that are expected not to be exceeded for normal procedures if normal practice performance is applied, otherwise investigation and appropriate corrective action should be taken [4].

Since the radiation exposure to humans should be always minimised, and since it is impractical to place dosimeters inside the human body, an alternative is the use of computational phantoms that enables a very precise assessment of organ doses [2].

The first reported phantoms were tanks of water or slabs of tissue equivalent materials which could hold dosimeters and allowed measurements 'in tissue'. These phantoms are still used for calibration of radiation detectors and treatment systems. However, as time progressed, health professionals have felt the necessity to simulate the human body with more accuracy, which led to development of anthropomorphic phantoms [1]. These phantoms provide a more realistic representation of the complex heterogeneity of the human body and, as a consequence, dose measurements more correlate with the dose distribution within the human body [1, 2].

Anthropomorphic models can be physical or computational. Physical anthropomorphic phantoms are made of solid materials radiologically equivalent to human tissues, nonetheless its use can be expensive and time-consuming due to necessary experimental and radiation safety procedures. Moreover, the number of commercially available physical phantoms is insufficient to represent the diversity of the

human population [2]. Therefore, computational anthropomorphic phantoms defined as computer models that aim to represent organs and tissues of the human body, at a given age, have been developed. Computational phantoms are advantageous since they can include extensive details of the exterior and interior features of the human body and can be manipulated in order to simulate inhomogeneities as tumours and calcifications and patient motion [2].

In the field of computational phantoms, three generations can be distinguished: stylized phantoms, voxel phantoms and boundary representation (BREP) phantoms. In the first generation of phantoms, organs are represented by primitives geometries as spheres, cylinders or prisms created by quadratic equations. Although all the improvements made in organs representation in stylized phantoms and their contribution to radiation dose evaluation, is perceptible that mathematical equations can not describe the complexity of the human body [5]. Hence, voxel phantoms were introduced in order to overcome stylized phantoms limitations about organs representations. These phantoms can be realised through computed tomography (CT), or magnetic resonance images (MRI) of real patients [2]. The development of a voxel phantom consists in processing tomographic data set in order to assign each pixel with a label that represents an organ. The phantom contains a huge number of tiny cubes designated as voxels grouped to represent different anatomical structures [2].

Since the computational approach is more versatile, efficient, precise and safer than the physical approach [1], the gold standard of radiation dosimetry would be to obtain a computational voxel model for each patient involved in radiation processes. A specific phantom for each patient would provided realistic and accurate dose measurements which helps to understand the risks and benefits of a radiation treatment or an imaging exam and provides dose optimisation, i.e., decrease of the dose without compromising image quality [1]. However, the development of a voxel phantom is still a demanding process from the computational time point of view.

Thus, the aim of this project is to develop and implement a computational voxel phantom starting by a physical one for precise organs doses assessment in the field of X-ray diagnostic (CT imaging). This work can be divided into two distinct parts: image segmentation and dosimetric calculations for phantom validation.

The goal of segmentation is to develop a simple, fast and accurate method able to extract the different radiosensitive organs of the human body. A segmentation approach fully or semi-automatic independent of the subject of the CT images would be the gold achievement of segmentation and a great improvement in development of specific voxel phantoms. Since the accuracy of dose estimates critically depends

on how well the anatomical models account for specific geometry and radiation attenuations properties of each individual, evaluation of segmentation performance and dosimetry calculations need to be executed.

The implementation process of computational phantoms has to comprise a validation step to evaluate phantom performance and the accuracy of organs doses. In this work, phantom validation is accomplished through dosimetry calculations. Dose measurements provided by an ionisation chamber (IC) coupled to a CT dose indexes (CTDI) phantom or to the physical anthropomorphic used might be compared to doses calculated by Monte Carlo (MC) simulations.

In this work, the voxel phantom was also be tested in order to perform image and dose optimisation. Therefore, anomalies as calcifications of different sizes, were inserted in the lung of the phantom, and the signal difference dose ratio was calculated to determine the optimal X-ray energy for lung imaging.

1.2 Thesis Outline

This dissertation is divided in eight chapters. **Chapter 1** presents a brief discussion of the problem of radiation exposure and the need of phantoms in order to evaluate radiation doses. The goals of dosimetry and radioprotection are also addressed in this chapter. Finally, the motivation and thesis organization are described.

Chapter 2 explains the problem of exposure to radiation due to CT examinations for human health, and, consequently the measures taken by international organisations for dosimetry and radioprotection. In this chapter, a brief review about the physical principles of CT and about the evolution of this technology is also presented.

The physical interactions between X-rays and matter and fundamentals of dosimetry are explained in **Chapter 3**.

Chapter 4 presents the advantages and disadvantages of direct and indirect methods to assess organ doses and report the use of voxel phantoms as a solution for accurate organs doses.

A review of segmentations methods for thorax's organs are briefly described in **Chapter 5**. A description of the two methods used in this project are included in this chapter. **Chapter 6** describes the materials as phantoms, CT systems and radiation detectors applied in this work. The summary of segmentation approach, MC simulations using PENELOPE code, and system validation can also be found in **Chapter 6**.

The results and discussion are presented in **Chapter 7**. Finally, general conclusions about this project and possible future work are discussed in **Chapter 8**.

Chapter 2

Computed Tomography

This chapter will focus on CT has a primary diagnostic imaging modality. The risks and the impact of CT as an increasing source of exposure to radiation will be discussed in Section 2.1. The role of international organisations on radioprotection and on the safe utilisation of radiation will also be discussed in this section.

Section 2.2 presents a brief description about the physical principles in the production of CT images, emphasising the most common image reconstruction algorithms used.

An overview about the technology developments in CT scanners over the years can also be found in Section 2.3.

2.1 CT as an increasing source of radiation exposure

CT, introduced by Hounsfield and Cormack in the 1970s, is a diagnostic medical exam that uses X-ray to produce multiple cross-sectional images of the inside of the body [6].

Due to technology developments, described in Section 2.3, CT has become a fast, minimal risk, painless and non-invasive procedure that allow acquisition of images with a level of image quality enough for a confident diagnosis [7]. However, CT involves larger radiation doses than conventional x-ray imaging procedures which appoint CT as one of the major contributor to the collective dose in the population [8] and have been a concern for health professionals.

2.1.1 CT examinations performed in Europe

The number of CT examinations prescript and the number of CT equipment available in hospital had a rapidly increase over the last decades, Figure 2.1. In fact, the Statistical Office of the European Communities (EUROSTAT) reported an increase of at least 1.0 units per 100 000 inhabitants in CT scanners available in Portugal, between 2009 and 2014, reaching a total of 228 CT scanner only in hospitals [9].

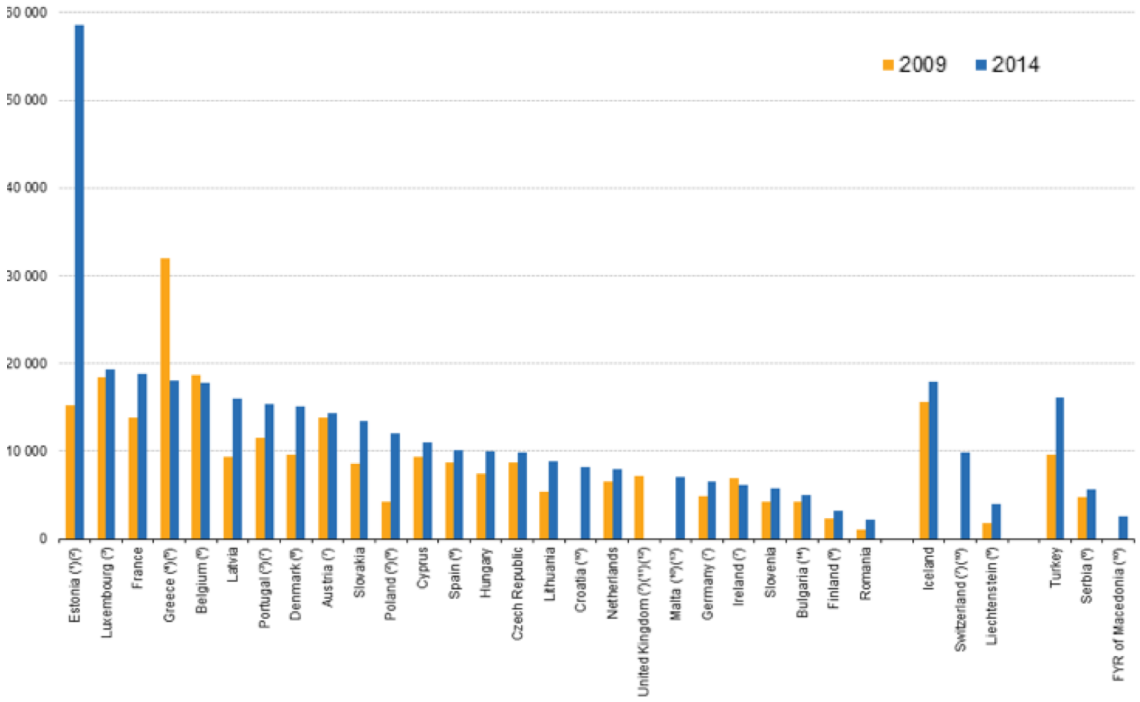

Figure 2.1: Number of CT scans performed in 2009 and 2014 per 100 000 inhabitants [9].

CT examinations can be used in diagnostic field in case of trauma or abnormality, to analyse anatomic characteristics as density or vascularisation, to plan and guide interventional or therapeutic procedures as guiding a needle during tissue biopsy or monitoring a treatment [7].

In line with the American College of Radiologists (ACR) appropriateness Criteria, i.e., the guidelines for health professionals that provide the most appropriate imaging or treatment decision for a specific clinical condition, CT is the recommended image modality in cases of occupational lung diseases as pneumoconiosis, mesothelioma [10], for screening of pulmonary metastases [11] or liver metastases [12] and for imaging a transcatheter aortic valve replacement [13].

2.1.2 Radiation Exposure

Besides the clear advantages and benefits that CT provides, health professionals are concerned with issues about the potential risk of radiation-induced malignancy. In fact, comparing the organ doses of CT examinations to the organ doses of conventional radiography, CT examinations involves higher doses of radiation, which contributes to an increase of the population dose exposure, Figure 2.2 [14]. According to Radiation Protection (RP) Nº180 report, the use of CT and plain radiography as diagnostic procedures contributes with 55% and 23%, respectively, to the total collective effective dose [15]. In Portugal, the contribution of CT examinations, in the diagnostic field, for the total collective effective dose increases to 74% [8].

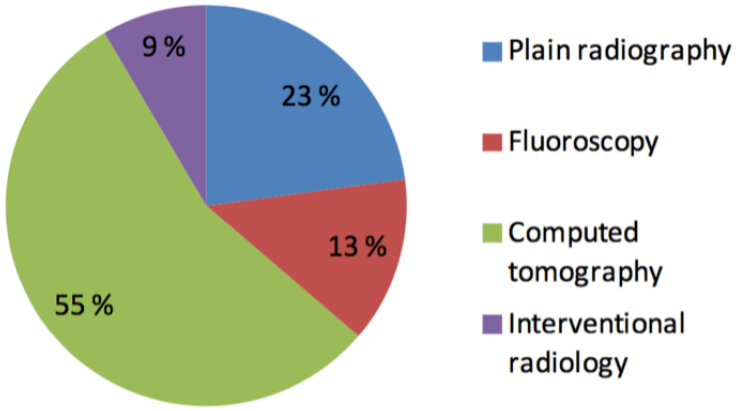

Figure 2.2: Contribution of the main groups of radiology procedures to the total effective dose. Adapted from [15].

Effective dose (explained in section 3.2.2) is a concept that reflects the effects and the risks of radiation in the organs and tissues that are sensitive to radiation and allows a comparison of radiation-induced risk among different examinations and background radiation [16].

Radiation effects can be distinguished in stochastic and deterministic depending on their dependency with dose. On one hand a deterministic effect only occurs if a threshold of exposure is exceeded and its severity increases as the dose increases [3].

On the other hand, a stochastic effect is dose dependent, occurs to any level of radiation exposure and the risks increase once the dose increases, therefore they can not be suppressed [3]. The relevant biological effect of stochastic effects is caused by energy deposition in biological tissues which can induce water ionisation and creates hydroxyl radicals that may interact with DNA causing damage and strand breaks.

Unrepaired strand breaks can lead to mutations, chromosome translocations and gene fusion associated to cancer induction[17].

Comparing to average background radiation, 3 mSv per year, the average effective doses estimated in European countries for chest, abdomen and trunk CT are, 6.56, 11.3 and 14.8 mSv, respectively, Figure 2.3 [15].

Although, radiation-induced risks are controversial at doses between 10 and 100mSv, health professionals are worried with patients who undergo multiple CT examinations and with paediatric patients, who besides having a longer lifetime for the effects of radiation to manifest, are more radiosensitive [14, 17].

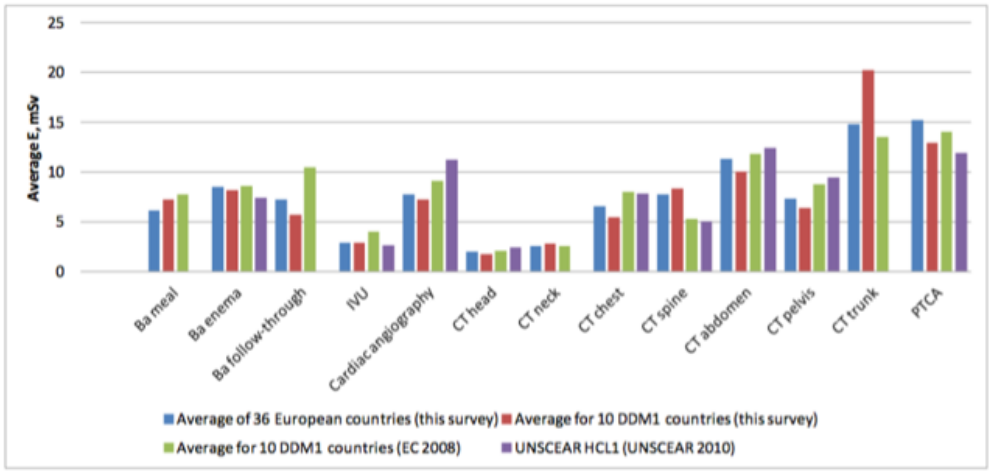

Figure 2.3: Average values of typical effective doses (mSv) for various CT examinations per body region. [15].

2.1.3 Measurements and Dosimetry

Associations as ICRP, International Commission on Radiation Units and Measurements (ICRU) and United Nations Scientific Committee for the Effects of Atomic Radiation (UNSCEAR) have been showing their concern about radiation-induced risks and radiation protection by publicising, over the years, regularly studies and reports containing scientific data, recommendations, safety standards and guides for a safe utilisation of radiation.

Since damage on genetic material may occur even at lower doses, which may not result in a visible tissue reaction but increases the risk of cancer many years later or hereditary diseases in future generations, is important to control exposure to ionising radiation [18].

In order to to minimise and control exposure, in 1991, ICRP established three fundamental principles of radiological protection defined in Publication 60 and re-

vised in ICRP 103. The first principle named as principle of justification assumes that any practice involving exposure to radiation carries a certain risk for patient and workers, thus, any examination needs to be justified and the benefit-to-risk ratio should be 'as high as reasonably achievable' (AHARA), in other words, an exam must be only performed if the outcome benefit overweight the potential risks [19].

Optimisation principle sets that exposure must follow ALARA principle, i.e., should be kept 'as low as reasonably achievable'. Optimisation is a challenge for physicians, once radiation dose is related to CT image quality and thereby to diagnostic accuracy. Use of lower doses may reduce signal-to-noise ratio (SNR), contrast and resolution which compromise diagnostic accuracy. Therefore, optimisation means finding the right dose level that can be applied in order to reach an adequate diagnostic quality [19].

DRLs are an example of an application of optimisation principle. DRLs, according to Council Directive 97/43/EUROTAM, are the dose levels defined for medical diagnostic radiology and nuclear medicines for typical examinations that are expected not to be exceeded in standard procedures when a good and normal technical performance is applied. These values selected by professional medical bodies in conjunction with national health and radiological protection authorities are established in 72% of 36 European countries as reported in RP N°180 [15]. The DRL value is derived from relevant regional, national or local data and is compared to the mean value or another appropriated value observed in practice for a reference group of patients or phantoms in order to help avoid radiation dose to the patient that does not contribute to the clinical purpose of a medical imaging task [20]. The dosimetry quantities used to set DRLs should be easily to measurable and vary according the imaging modality [21, 22]. For radiography, DRLS are given in terms of air kerma-area product ($mGy.cm^2$) and entrance surface air kerma (mGy). For fluoroscopy and interventional radiology procedures the quantities used to define DRLs are air kerma-area product ($mGy.cm^2$), air kerma at patient entrance reference point (Gy), fluoroscopy time and number of images. On the other hand, mammography and breast tomosynthesis use quantities as incident air (mGy), entrance surface air kerma (mGy) or mean glandular dose (mGy). For nuclear medicine, DRLs are set in activity administered to patient, and/or in administered and activity per kg of body mass. Finally, for CT, DRLs can be given in terms of Dose Length Product (DLP – mGy.cm) or in terms of pitch corrected CT Dose Index (CTDIvol mGy) [21, 22]. In terms of DLP, the DRL range for a chest routine CT is between 270 and 700 mGy.cm while for a high resolution chest CT (HRCT) is between 80 and 300 mGy.cm. On the other side, in terms of $CTDI_{vol}$, for a routine Chest CT the most

common value for DRL is 10 mGy in a range from 10 to 30 mGy [15]

Dose and Risk limitation principle, the latest principle established by ICRP 60, implemented effective dose limits for workers and members of public for different radiosensitive organs as skin and eyes, for example [4].

2.2 Technology and Physics principles

The term CT is also used to refer to a computed X-ray imaging procedure in which an image of a region of interest is reconstructed based on the intensity profile of X-rays in that area [23]. CT images are a result of radiation intensity attenuation sum in every volume element between source and detector that is crossed over by an X-ray beam. The gantry, a major component of the CT scanner, incorporates the X-ray tube and the detector and rotate around the patient in order to measure the transmitted photons from the patients and the intensity of X-rays from the X-rays tube [23]. The intensities measured at different positions of the X-ray tube create an intensity profile whose projection gives information about the attenuation profile [24].

The attenuation data gathered during rotation of the gantry is sent to a computer that reads the information and generates a digital image by applying reconstructions algorithms [24].

The result of the reconstruction algorithms of a slice is designed as an image matrix that ranges in size from 256×256 to 1024×1024 where each pixel corresponds to the attenuation data converted into CT numbers [25]. The relation between tissue attenuation, μ , and CT number was established by Hounsfield and is calculated using the following equation [23]:

$$HU = 1000 \times \frac{\mu_{tissue} - \mu_{water}}{\mu_{water}} \tag{2.1}$$

The matrix of CT numbers forms the digital image that can be displayed in a computer screen. The available range of CT numbers varies between scanners and available bits per pixel, in case of 12 bits the range is from -1024 to 3071 HU [25]. The HU value of each pixel, assigned with different tons of grey, reflects the material density and the attenuation characteristic of tissue [26].

The HU value increases with tissue density and material effective atomic number, high HU number means higher attenuation, assigned with white and lower HU values are darker, Figure 2.4.

Since the human eye can only distinguish a limited number of grey levels, to

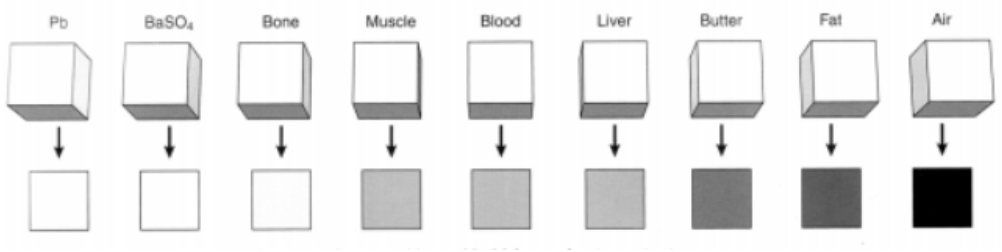

Figure 2.4: Radiosensitivity as a function of composition, with thickness kept constant [27].

enable a more detailed visualisation between structures with small differences in CT numbers, just a portion of CT scale is displayed [25]. This process, in CT, is defined by window width (WW) and of the window level (WL), the centre of the range, in order to enhance contrast and brightness of the image, respectively [25], Figure 2.5.

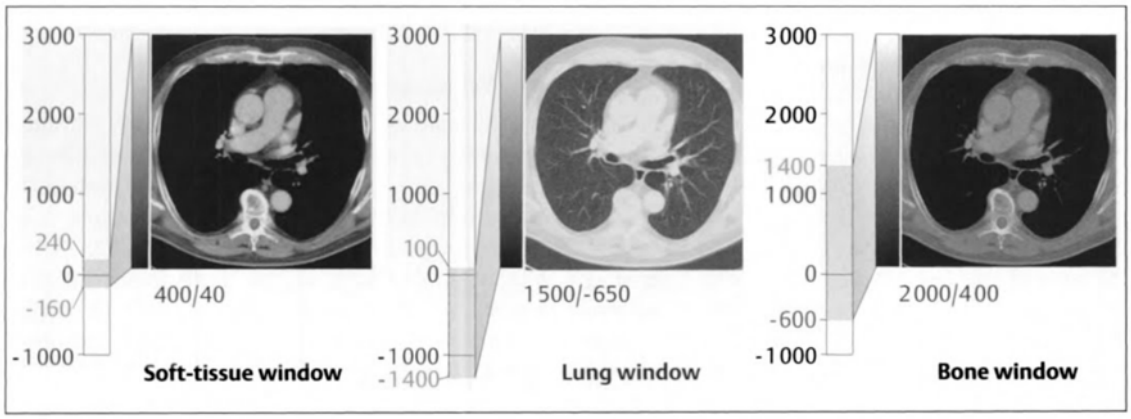

Figure 2.5: Effect of window level and window width on image brightness and contrast on a Chest CT slice. (a) Soft Tissue window, (b) Lung window, (c) Bone window. Adapted from [25].

2.2.1 Image Reconstruction Algortithms

Image reconstruction in CT is defined as the process of finding the two-dimensional distribution of the attenuation, μ , from the projection information acquired and stored as sinograms. A sinogram is a set of projection of a single slice where each point is defined as the reading of a detector at a projection angle θ [23].

Image reconstruction algorithms aim to propagate the sinogram back to the image space, using backprojection that reconstructs from projection by applying central slice theorem (CST). CST involves three different domains: image, Radon and Fourier domain by stating that the value of the two dimensional Fourier Trans-

form (FT) of $\mu(x,y)$ along a line with inclination θ is given by the uni-dimensional FT of the profile of the sinogram acquired at angle θ.

While the two dimensional FT of the image is given by

$$F(\eta,\xi) = \int\int f(x,y)e^{-j2\pi(\eta x+\xi y)}dxdy \tag{2.2}$$

The FT of the projection is

$$P_\theta(\omega) = \int p_\theta(t)e^{-j2\pi\omega t}dt \tag{2.3}$$

$$p_\theta(\omega) = \int f(x,y)\delta(xcos\theta + ysin\theta - t)dxdy \tag{2.4}$$

Knowing the Randon Transform of the projection, Equation 2.4 and replacing in Equation 2.3, the CST is proved and image can be reconstructed.

Filtered backprojection (FBP) is a technique used on CT image reconstruction based on the assumption that the measurements and the projection data are represented by continuous functions. Filtering occurs before backprojection in order to correct the low pass blur due to the different number of projections passing through the centre and the periphery of an object [28].

Therefore, a high-pass filter is applied to measured data to enhance small detail and sharp edges and to ignore smooth areas [23]. Since image sharpness are directly coupled to image noise, the choice of the filter (kernel) used to compensate the effect of the low-pass blur, has to be based on the compromise between spatial resolution and image noise [28].

Besides of being robust and fast, FBP can be affected by image noise due to reduction in radiation dose, artefacts or poor low contrast detectability since it ignores information about X-ray photon statistics as Poisson distribution of photons [28].

In order to reduce radiation dose while improving quality image reconstructions algorithms, namely iterative reconstruction algorithms, were introduced [29]. As the name suggests, these algorithms are based on iteration cycles. First, an initial estimation of the projections of the volumetric object is created to be compared to the acquired data. The comparison is associated to an error, which is back projected to deduce a correction term to adjust the estimation [30]. The iterative process: forward projection, comparison, back projection and adjustment is repeated until a fixed number of iteration is reached or a quality criterion in the image estimated is

fulfilled [30].

A scheme of the process cycle of FBP and IR algorithms are illustrated in Figure 2.6 [23].

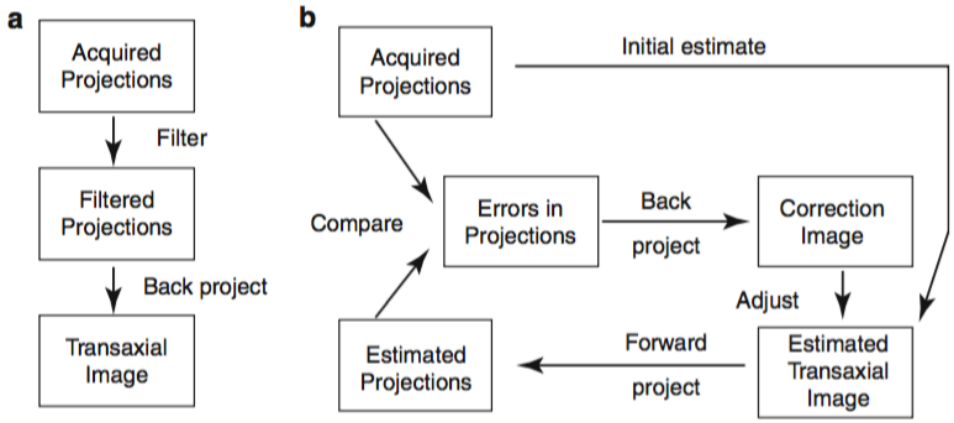

Figure 2.6: CT image reconstruction methods: (a)FBP (b) IR. Adapted from [23].

IR techniques have been studied as a beneficial tool to decrease radiation dose in CT examinations without compromising image quality and diagnostic information, which is attractive in lung [31] and colorectal cancer examinations, perfusion studies [32], paediatric imaging [33] and for repeated examinations [28]. However, due to the familiarity of the medical imaging community with the use of FBP, and to the acceptance of the limits of FPB algorithm by the radiologists and others CT users and buyers, FPB remains the most adopted algorithm in clinical use [34].

2.3 Technology Review (Past and Present)

Since its introduction in 1971 by Godfrey Hounsfield, the technology of CT has evolved. The first generations of CT, also known as conventional CT, were based on a slice by slice axial sequential scanning. In other words, was a start and stop system where the X-ray tube was fixed and rotated around the patient to collect data from a single slice of tissue, followed by a movement of the patient table in order to scan a contiguous slice [24]. To overcome the limitations of the conventional scan, as longer examinations times and omission of certain portions of the anatomy (misregistration of slices), the single slice CT (SSCT) was introduced. SSCT incorporates slip rings technology, i.e., electromechanical devices consisting of circular electrical conductive rings and brushes that allow transmission of electrical energy across a rotating interface [23]. Thus, instead of an acquisition slice by slice,

the gantry can rotate continuously while the patient table moves through the gantry creating a helical path [24]. The name single slice arises from the 1-dimensional array of detectors that acquires one slice per rotation [24].

Multislice CT scanners (MSCT) appeared as an upgrade of the SSCT. Instead of using a single row detector that limits volume coverage speed, in this new generation each of the individual detectors elements in the z-direction is divided into smaller detectors elements, forming a 2-dimensional detector array, Figure 2.7 [35]. The advantage of these detectors is that a detector with n rows, will be n times faster, since it can acquire more information and more slices in shorter time intervals [23].

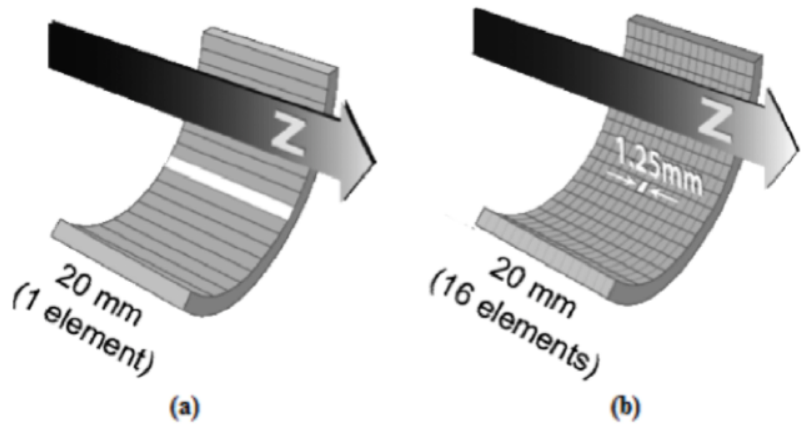

Figure 2.7: Comparison between a (a) CT system with a single row of detectors and (b) a CT scanner with 16 rows of detectors with thickness of 1,25 mm. Adapted from [36].

The MSCT detectors can be categorised as *matrix array detectors* or *adaptive array detectors*. While matrix array detector refers to a fixed or isotropic array detector that contains several channels or cells with the same dimensions, an adaptive array detector is anisotropic, i.e., the channels or cells have different sizes [23]. Thus, in MSCT the slice thickness is determined by the detector design and not by the x-beam collimation as in SSCT [35].

With MSCT is possible to perform helical scanning or axial scanning. In helical scanning the rotation of the X-ray tube and the movement of the table occur simultaneously with continuous data acquisition as in SSCT. On the other hand, in axial scanning a slice is acquired during one single 360º rotation of the X-ray [35].

For SSCT the term *pitch* refers to the distance travelled by the table per rotation of the X-ray tube, $T(mm)$, to the width of the X-ray beam, $W(mm)$, however this concept has emerged to *pitch ratio* for MSCT scanners [23]. In this new definition, *pitch ratio* is given by the table movement per rotation divided by the total thickness of all of the simultaneously acquired slice. The total width corresponds to the

sum of the individual thickness of each slice, i.e., the number of slices, n times the individual thickness, T [35]. Higher values of *pitch ratio* are related to faster acquisitions and lower doses. Nevertheless ratios lower than 1 mean higher doses, the image quality is improved and, consequently, the information about small details in anatomy structures is better.

Dual-source CT uses an additional attenuation measurement acquired at a second energy in order to differentiate and quantify material compositions with similar CT numbers [37]. Two technical approaches can be distinguished: dual source scanner with dual detector arrays and with single-source scanner [38]. As the name suggests, on dual-source scanner, two separate x-rays tubes operate simultaneously at two different tube potentials (a higher potential at 120 or 140 kVp and a lower potential at 100 or 80 kVp) and two detector arrays are used to acquire two different image datasets [38]. On single-source CT scanner two types of detectors are being studied: a single detector layer, already used in clinical, and a dual detector layers. A single-source CT scanner with a single detector array relies on a single X-Ray source with fast switching between two kilovoltage settings (80 and 140 kVp). On the other side, on a single-source dual CT scanner the detector array is modified with two scintillation layers arranged one atop the other to receive separate high-and low energy image data [38].

Photon-counting detectors have been studied as the most robust solution to dual or multi energy acquisition with potential to revolutionise CT imaging [39]. Such detectors aim to count discrete photons interactions based on the choice of energy thresholds and the associated energy of each photon. Thus, photons would be registered within specific energy thresholds data sets which enable reading data of only specific energy ranges and consequently, allow the rejection of counts due to measured electronic noise [37]. If these detectors do become available will offer several advantages, including improvement of spectral separation allowing multi-energy CT, increase of dose efficiency by decreasing electronic noise and optimisation of the contrast-to-noise ratio [37, 39].

Chapter 3

Diagnostic Radiology Physics

In 1895, Wilhelm Conrad Roentgen discovered a new form of electromagnetic radiation that enabled the visualisation of anatomical structures of a human body. The discovery of X-rays represented a huge contribution to the evolution of medical imaging, and, over time, several medical imaging systems were created and improved (e.g. CT scanners, radiography).

In this chapter, a brief explanation about the types of interaction of photons with matter, which constitutes the basis for X-ray imaging, is reported. In addition, some basic theoretical concepts of dosimetry in the diagnostic field are presented.

3.1 Interaction of photons with matter

Photons are considered indirectly ionising radiation since their energy is, firstly, transferred to a charge particle and then is deposited in the absorbing medium by the charged particle. When a photon passes through a medium three scenarios may occur: (1) the photon passes without interacting with the material, (2) the photon is totally absorbed by the medium or (3) during interaction, photon deposits some of its energy and changes its trajectory [40].

Depending on photon energy, density and atomic number of the medium, photons may interact with the nuclei or with an orbital electron. Photons can interact with the medium through photoelectric effect with full photon absorption, Rayleigh and Compton effect associated with elastic ad inelastic scattering respectively, and pair production, if the photon energy is converted into an electron-positron pair. In radiodiagnostic field the energy of X-Ray used is higher than 15 KeV and lower than

150 KeV [41]. Therefore, in this study, the range of X-ray photons used is from 30 KeV to 120 KeV. Since pair production effect only occurs for energies higher than 1.022 MeV, this effect is negligible in CT imaging [40].

3.1.1 Cross Section

Cross section, σ, can be defined as the mutual area where two particles interact and is used to express the probability of collision between an accelerated beam of one type of particles with another type of particles.

As mentioned above, different photons coming from the same beam may interact with electrons through several processes each of them associated with a differential cross section. The probability of a process occurring depends strongly on variables as density of the target material, energy of the photon and atomic number of absorber, Figure 3.1 [42].

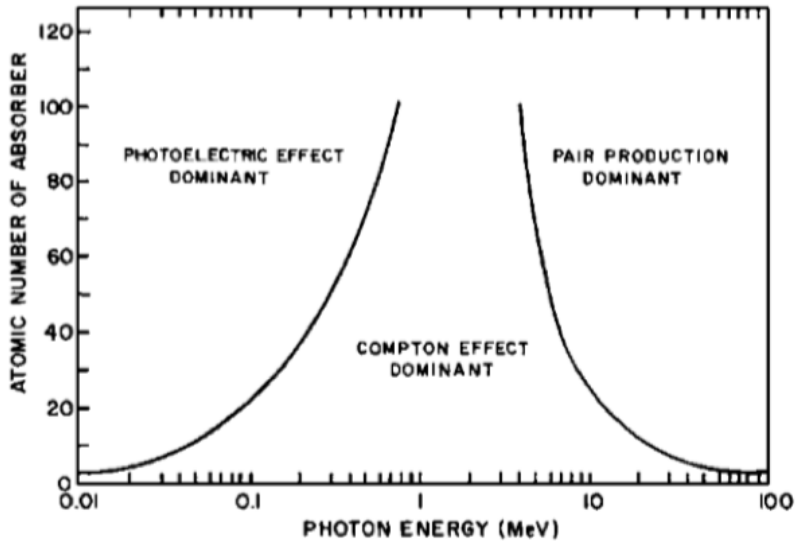

Figure 3.1: Relative importance of the three principal interactions of x and rays. Adapted from [42].

The differential cross section is given by,

$$\frac{d\sigma}{d\Omega} = \frac{dN}{\Phi} \tag{3.1}$$

where dN represents the number of particles per unit of time, Ω is the solid angle and Φ the incident flux. The total cross section is expressed in barn $1b = 10^{-24} cm^2$ and is obtained integrating the previous equation for all solid angles, Equation 3.2.

The differential cross section is given by,

$$\sigma = \int \frac{d\sigma}{d\Omega} d\Omega \tag{3.2}$$

3.1.2 Attenuation coefficients (linear and mass)

As aforementioned, a fraction of the total number of photons transverse the medium without interacting or losing energy. For a monoenergetic beam, the number of photon that passes through a material of thickness is expressed by the Beer-Lambert law, Equation 3.3:

$$I = I_0 e^{-\mu x}, \tag{3.3}$$

μ is defined as the product of the number of atoms per unit of volume, N_a, with the total cross section per atom, σ. The μ, known as linear attenuation coefficient has dimensions of inverse of length, cm^{-1} and depends on the type of interaction, energy of incident photon beam and physical state of the absorber. Thus, the total cross section, σ, is obtained by summing the cross sections for each process of interaction: coherent scattering (ω), photoelectric absorption (τ), pair production (κ) and photodisintegration (φ), Equation 3.4

$$\sigma = \sigma_\omega + \sigma_\tau + \sigma_\kappa + \sigma_\varphi \tag{3.4}$$

Mass attenuation coefficients results from the division of the linear attenuation coefficients by the density of the absorber medium, $\frac{\mu}{\rho}$, and its SI units are square meters per kilogram m^2/kg. This quantity can also be calculated when the absorber material is composed by different compounds using the following formula:

$$\frac{\mu}{\rho} = \sum_i (\frac{\mu}{\rho})_i w_i, \tag{3.5}$$

where w_i represents the weight fraction of the different compounds [42].

3.1.3 Photoeletric Effect

During photoelectric interactions, an incident photon with initial energy, E_0, collides with a bound electron and transfers all of its energy. As a result of this collision the bound electron, also referred as photoelectron, is ejected with kinetic energy, E_k, equals to the difference between the initial energy and the binding energy

E_b, i.e., the energy required to remove the electron, Figure 3.2 [43]

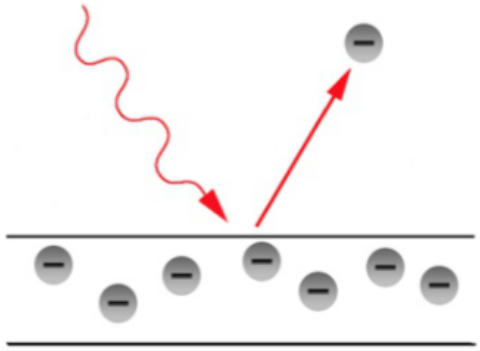

Figure 3.2: Schematic diagram of photoelectric effect. Adapted from [44].

Mathematically, this process is described by Equatio 3.6:

$$E_k = E_0 - E_b. \tag{3.6}$$

According to Planck, the initial energy of the photon can be expressed by the photon energy or the photon wavelength: $E = h\nu = \frac{hc}{\lambda}$, where h is the Planck's constant, ν is the photon frequency, c is the speed of light and λ represents the wavelength [42].

The injection of an electron of the inner shells leaves a hole that needs to be filled immediately. Consequently, the atom undergoes electronic reorganisation producing characteristic photon (florescence) and Auger electrons. The sum of X-ray characteristic and Auger electrons energies equals the binding energy of the ejected photoelectron [42].

As can be seen in Figure 3.1, the photoelectric effect cross section, σ_τ, is a function of the photon energy, E_0, and of the atomic number Z of the absorber. The probability of photoelectric interaction decreases rapidly as the photon energy decreases but increases with increase of Z, Equation 3.7.

$$\tau \sim \frac{Z^4}{E_0^3} \tag{3.7}$$

3.1.4 Rayleigh Effect

In Rayleigh or coherent scattering, incident photons are scattered or deflected due to an interaction with bound electrons. The amount of energy transferred to the absorber material is insufficiently to excite or ionise the atom, resulting in relatively

small angles of deflection and a return of the orbital electrons to their original state. However, can be noticed a difference in energy between the incident photon and the scattered photon. Despite of being almost negligible, the small fraction of energy deposited in the material contributes to the reduction of resolutions in CT examinations [42].

Rayleigh effect becomes more important as the photon energy decreases and the atomic number, Z, of the medium increases [43].

3.1.5 Compton Effect

Whereas the incident photon in photoelectric effect and in coherent scatter hits a bound electron, Compton effect occurs, mainly, in free individual electrons. If the photon energy is similar to the binding energy, photoelectric absorption is more probable to occur [43].

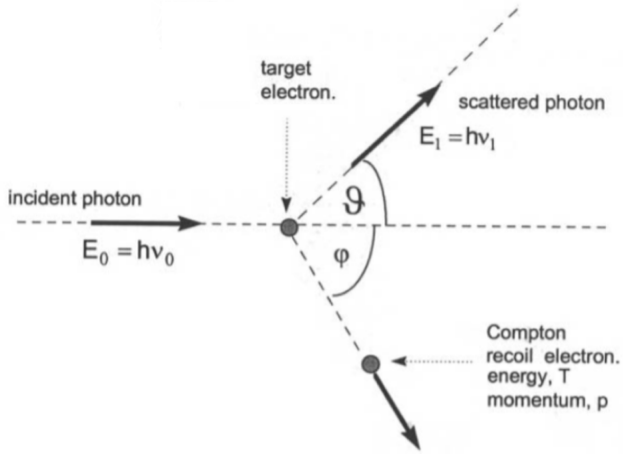

Figure 3.3: Schematic diagram of Compton collision. Adapted from [43].

Figure 3.3, describes Compton effect, also referred as incoherent scattering. A photon with initial energy, E_0, hits a free electron or a bound electron with binding energy lower than E_0, and a fraction of its energy is transferred. The initial photon retains part of its energy during collision and is scattered with an angle, θ . The recoil electron is also scattered with an angle, φ, and an energy equals to the amount of energy lost by the photon. On one hand, if a low energy photon undergoes a Compton interaction only a small part of its energy is recoiled by the electron. On the other hand, when the incident photon is considered of high energy, only a small fraction of its energy is retained by the photon [42].

The energy of the scattered photon is expressed using the laws of the conserva-

tion energy and momentum:

$$E' = \frac{E_0}{1 + \frac{E_0}{m_0 c^2}(1 - cos\theta)} \tag{3.8}$$

In Equation 3.8, $m_0 c^2$ corresponds to the rest-mass of the electron and is a constant value equal to 511 keV. Using the same assumptions, the relationship between angle θ and angle φ is given by:

$$cot\theta = (1 + \frac{E_0}{m_0 c^2})tan\frac{\varphi}{2} \tag{3.9}$$

As referred, Compton interactions occur primarily with unbound electrons, consequently, Compton mass attenuation coefficient increases as the atomic number of the absorber, Z, increases. On the other side, photon attenuation due to Compton interaction decreases as photon energy increases [43].

3.2 Dosimetry Units

CT and conventional radiography can be distinguished by dose distribution inside the patient. In conventional radiography the dose decreases continuously with the penetration in the patient body. On the contrary, in CT due to its rotational geometry, the dose is almost equally distributed in scanning plane.

Therefore, there are several quantities used to evaluate and quantify the amount of radiation absorbed during a CT examination. These indicators, describe in the following sections, can be categorised in two categories: local dose quantities and integral dose quantities. Local dose quantities as CTDI, dose free-in-air and organ doses, are indicators of intensity of the irradiation inside the limits of the irradiated body region. DLP and effective dose are considered integral dose quantities as they give information about the total amount of radiation absorbed during a CT examination [45].

3.2.1 Kerma

Kerma (K) stands for *Kinetic Energy Released in the Material (or per unit Mass)* and by taking into account the secondary ionisation, represents the sum of initial kinetic energies of all charged particles released in the medium.

$$K = \frac{dE_{tr}}{dm} \tag{3.10}$$

Kerma value is measured in Gray (Gy) or in J/kg and is given by the sum of two components: the collision kerma, K_{col}, and the radiative kerma, K_{rad}. The first, K_{col} translates the amount of energy released to charge particle as electrons per unit mass that is deposited locally resulting in ionisations and excitation collisions. Radiation kerma, K_{rad}, is related with the secondary electrons of high energy and the consequently production of penetrating Bremsstrahlung radiation due their interactions.

$$K = E_{col} + E_{rad} \tag{3.11}$$

The relation between the total kerma and the collision kerma can be expressed in terms of the bremsstrahlung fraction,$\bar{g}$, 3.12 [43]

$$K_{col} = K(1 - \bar{g}) \tag{3.12}$$

3.2.2 Absorbed, equivalent and effective dose

The amount of energy deposited in unit mass of tissue due to radiation exposure is defined as **absorbed dose** (D). With units of Gray (Gy), D is a dose indicator independent from radiation type and tissue irradiated [23].

$$D = \frac{E_{abs}}{dm} \tag{3.13}$$

However, the effect of radiation on the tissue absorber depends on the nature of radiation. Thus, for each type of incident radiation (neutrons, gammas and x-rays, protons) is assigned with a weighting factor, W_T, that quantifies the risk of exposure to specific radiation was introduced. **Equivalent dose**, H_T, given in Sieverts (Sv) is a result of the multiplication of the absorbed dose by the weighting factor. X-rays have a weighting factor of 1 [23].

$$H_T = \sum DW_T \tag{3.14}$$

Besides the type of radiation, organ doses are also related with the type of tissue. Some organs are more susceptible to ionising radiation than others. The tissues sensitivity is quantified by tissue weighting factor, W_R, and are independent from the type or radiation and energy. **Effective dose**, E , obtained by the following

formula describes the dose delivered in a certain organ or tissue:

$$E = \sum H_T W_T = \sum W_T \sum W_R D_{R,T}(Sv) \tag{3.15}$$

While dose measures the amount of energy deposited within the volume of interest, kerma takes into account the energy transferred to secondary particles due to interactions of incident radiation. The relationship between these quantities is expressed as:

$$D = \beta K_{col} = \beta K(1 - \bar{g}) \tag{3.16}$$

Where β is a constant of proportionality. In diagnostic field, the secondary particles, electrons, have low energies, thus, they are absorbed almost in the same region where the interactions occur, and, consequently, β equals to 1 [46].

3.2.3 Exposure

Originally defined by Roentgen as 1 e.s.u as the charge liberated in $1cm^3$ of dry air, exposure, is nowadays, a quantity used to measure the ability of a radiation field to ionise air. The SI units of exposure is Roentgen (R) equivalent to $2.58 \times 10^{-4} C/kg$ [43].

3.2.4 CTDI, $CTDI_{100}$, $CTDI_{weighted}$

CTDI is a standard output quantity of radiation dose in CT scanners that allows comparison between different scanner systems.

Since the dose in a particular slice is increased due to contributions from neighbour's slices, Food and Drug Administration, FDA, defined CDTI as the sum of all dose contributions along a line parallel to the axis of rotation of the scanner.

$$CTDI = \frac{1}{Nh} \int D(z) dz, \tag{3.17}$$

where N represents the number of slices acquired, h , the slice thickness and $D(z)$ represents the dose distribution profile [45].

This definition was accepted by the International Electrotechnical Commission (IEC), who extended the length of the examination measurement to $100mm$. $CTDI_{100}$ is the level of absorbed dose measured at the centre of the gantry using a

$100mm$ Ion chamber detector, [23]

$$CTDI_{100} = \frac{1}{Nh}\int_{-50mm}^{+50mm} D(z)dz \tag{3.18}$$

$CTDI_{100,air}$ can be measured, for example, using two polymethyl methacrylate phantoms (PMMA), one of $16cm$ for head and another of $32cm$ for trunk. Knowing that the dose decreases from the surface to the phantom centre, $CTDI_{weighted}$ can be calculated as a weighting between the $CTDI_{100}$ measured at the centre of the phantom and the $CTDI_{100}$ measured at the periphery, Equation 3.19:

$$CTDI_w = \frac{1}{3}CTDI_{100,centre} + \frac{2}{3}CTDI_{100,periphery} \tag{3.19}$$

For spiral or helical scanners, $CTDI_{vol}$ can be calculated dividing the $CTDI_w$ by the pitch, i.e., the distance travelled by the table per rotation, which besides the dose in the x-y axis also considers the dose in z-axis.

3.2.5 DLP

Another dose descriptor used in CT dose studies is DLP, which relates $CTDI_{vol}$ with examination length, l providing information about the amount of exposure for a CT exam with a specific length of irradiated volume [23].

$$DLP = CTDI_{vol} \times l \tag{3.20}$$

DLP is measured in $mGy.cm$, and is directional dependent on examination length.

Chapter 4

Organ Doses Assessment

Since CT has become a primary diagnostic tool, patient dose and the concern about how to quantify organ doses have gained interest. In 1970s, when the first CT was introduced the patient dose was relatively low (effective dose of approximately 1.3 mSv) and limited to the brain. However, the introduction of the whole body CT in the 1980s and the advance of spiral volumetric CT, in the 1990s, contributed for the spreading of CT applications, for improvement of X-ray power and volume scanned and, consequently, for the increase of patient dose [19].

Organ doses have been used by physicians and radiologists to predict and estimate the probability of deterministic and stochastic effects occur in patients who undergo exposure to radiation.

This chapter focus on the development of computational voxel phantoms for MC simulations and organ dose assessment. In addition, the importance and evolution of phantoms, either physical or computational, and a brief review of direct and indirect methods is also presented in this chapter.

4.1 Estimation of organ doses: direct and indirect methods

In order to respect ALARA principle and to clarify the viability of a CT examination is important to track the individual patient radiation exposure and estimate organ doses. The dose received during a CT examination depends on the scanner type/manufacture, on the scanning protocol (kVp and mAs) applied as well as on

the length of the region scanned, tube rotation speed, helical pitch, collimation, filtration, patient weight and patient size [47].

The radiation dose absorbed by the organs and tissues of the body, during a CT examination, can be measured by indirect and direct methods. In direct methods dose is measuring on patient or humanoid phantoms by using an IC or small devices as thermoluminescents dosimeters (TLDs). On the other side, in indirect methods, doses are estimated through measurement of CTDI and published conventional factors obtained from MC simulations and mathematical phantoms [47].

In spite of being good dose descriptors and a reliable measure of the dose output of a CT scanner, $CTDI_{100}$, $CTDI_{vol}$ and DLP are object independent measurements that give information about radiation output of a system and allow comparison between different systems but do not reflect patient organ doses [19]. While $CTDI_{vol}$ is calculated as a weighted average dose over a cross section of a standard cylindrical acrylic phantom, estimation of organ doses requires using tissue weighting factors or conversion factors. [48].

In 2011, a group of investigators of American Association of Physicists in Medicine (AAPM) proposed size-specific dose estimates (SSDE), a parameter that considers patient diameter and converts the $CTDI_{vol}$ provided for a CT scanner into patient dose, Equation 4.1 [19].

$$SSDE = f \times CTDI_{vol} \tag{4.1}$$

The conversion factors, f, are based on the thickness of the patient's torso and derived from four different measurements: the anteroposterior dimension (AP), the lateral dimension (LAT), the sum of AP and LAT and the effective diameter calculated by taking the square root of the product of AP and LAT [48].

Even if SSDE provides a quick estimation of patient dose, specific organ doses remain a difficult task. Unfortunately, dose inside a living person cannot be measured directly, and for this reason, several approaches as use of physical an computational phantoms have been developed. [2, 19].

Recent studies, present a new direct method for organ dose measurements using embalmed cadavers as a substitute for living patients. According to Griglock [49], this approach is more anatomically accurate comparing to the use of physical phantoms. The cadavers were embalmed and optically stimulated luminescent dosimeters (OSLDs) were placed in the organs of interest. Different clinical protocols as chest-abdomen-pelvis, chest, abdomen and three phase liver were performed

using a CT scanner to the model. Study's results indicate that dosimeter placement system provides precise and reproducible access to internal organs without losing anatomic integrity. Consequently, the radiation attenuation properties and organ doses evaluated in post-mortem subjects give relevant and reliable dose information for CT patients.

4.2 Phantoms

In the radiation protection community, the term phantom refers to an anatomic model that can be physical or computational. While physical phantoms are constituted by solid materials equivalent to human tissues, computerised models can be defined by equation-based mathematical function, digital (voxel-based) volume arrays, or hybrid equation-voxel models [2].

4.2.1 Physical Phantoms

As aforementioned, physical and computational phantoms represent a precious tool to estimate doses inside the human body. Physical phantoms can be cylindrical or spherical as the CTDI phantom also designed as polymethyl methacrylate (PMMA) phantom used to measure CTDI, or anthropomorphic as, for example, CRIS ATOM phantom [50] or the Kyoto PBU-60 [51] used in this study.

Physical phantoms are used to estimate organ doses, assure quality control, validate dosimetry tasks and measure important CT dose quantities as $CTDI_w$.

While solid phantoms as PMMA or water phantoms are made of solid materials radiologically equivalent to human tissues without a specific shape or size, materials in anthropomorphic phantoms have densities and shape similar to human organs and bones [2, 19].

Therefore, normally, for estimation of organ doses anthropomorphic physical phantoms are used, since the modulation of their constituents into organs and bone shapes allows a better and more realistic representation of the human body [52]. However, the use of anthropomorphic phantom has some disadvantages, it is a technique a bit expensive and time consuming and the dose values are, commonly, measured at the surface of the phantom. Furthermore, the diversity of human population can not be represented by the limited number of body sizes available.

4.2.2 Computational Phantoms

Since the 1960s, computational phantoms have evolved to overcome physical phantoms limitations. Computational phantoms include detailed information such as shape, volume, mass, density and chemical composition of radiosensitive organs and tissues and enable, accurate, simulations of radiation interactions and energy deposition patterns in the body.

The number of computational phantoms reported in studies of radiation protection, medical imaging and radiotherapy have been increasing in the last decades, reached a total of 121 phantoms in 2009, Figure 4.1.

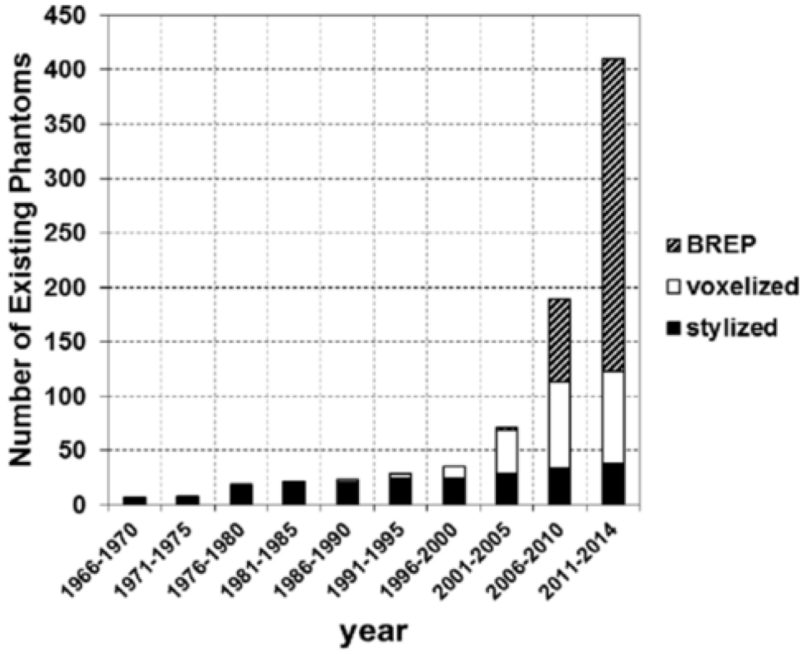

Figure 4.1: Exponential growth of the number of computational phantoms in existence since 1966. Adapted from [2].

To create a computational phantom several factors as anatomy, radiosensitivity of organs/tissues, computational efficiency and geometrical compatibility with MC code should be taken into account. Three generations of phantoms can be distinguished based on their construction method (see Figure 4.2): stylized phantoms formed on constructive solid geometry (CSG), voxel and BREP phantoms created from tomographic images. BREP phantoms are also based on advanced primitives, used to generate surfaces of the organs in which radiation interactions and energy deposition occur.

While CSG method uses Boolean operators to combine primitives shapes as

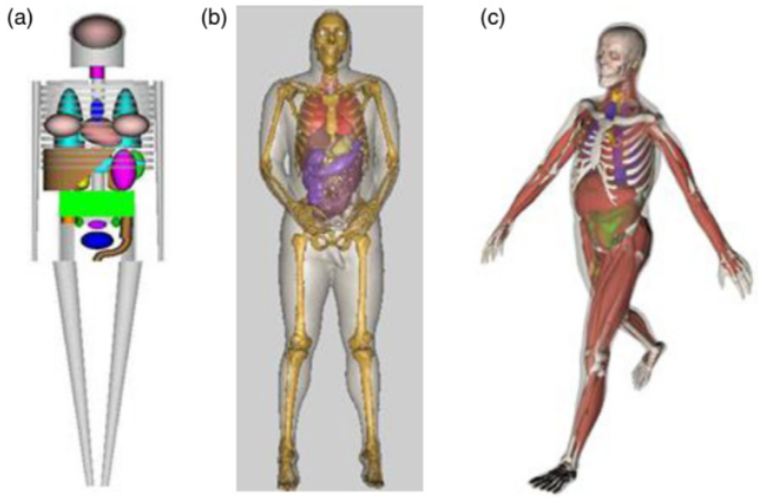

Figure 4.2: Three generations of phantoms. (a) Stylized Phantoms. (b) Voxel Phantoms (c) BREP phantoms. Adapted from [2].

spheres, prisms, cylinders, cuboids or cones that can be described by quadratic equations, BREP relies on topological information that provides relationship among vertices, edges and faces and on there orientation. In BREP phantoms the exterior of an object/organ is defined as non-uniform rational B-spline (NURBS) which involve surface contour extraction of the different organs [1]. BREP method is more advantageous and flexible, once it has more operations tools available, such as surface deformation that can be used to adjust organ size and to simulate organ motion [2].

4.2.2.1 Stylized Phantoms (1960s-2000s)

The first generation of phantoms, so-called stylized phantoms, were primarily developed for internal dosimetry using radionuclides. In 1959s, the ICRP reported a simple model using CSG modelling techniques where each organ was designed as a sphere with an *effective radius* and the radionuclide of interest, radium, was placed at the centre of the sphere. The *effective absorbed energy* calculated for each organ was reasonably accurate.

A year later, in 1960s, Fisher and Synder from the Oak Ridge National Laboratory (ORNL) developed an adult male phantom with three regions: head and neck, trunk including arms and the legs shaped as elliptical cylinders and cones. In 1969, the first heterogeneous phantom, Medical Internal Radiation Dosimetry-5 (MIRD) was released. This phantom was composed of a skeleton, a pair of lungs and soft tissue and intended to represent a healthy 'average' adult male, also known by reference man. Despite its limitations, the internal organs had a crude represen-

tation, this hermaphrodite phantom was used as a reference to develop a family of phantoms consisted of an adult male, a new-born and individuals of 1, 5, 10 and 15 years old and a pair of gender specific adult phantoms (called ADAM and EVA).

These phantoms, from the outside view have the appearance of the human body, however, although organs features were adjusted in order to correct size, position, composition and density, their shape was simplified and modelled using mathematical equation, which are insufficient to describe and model the complex of human anatomy [2], Figure 4.3.

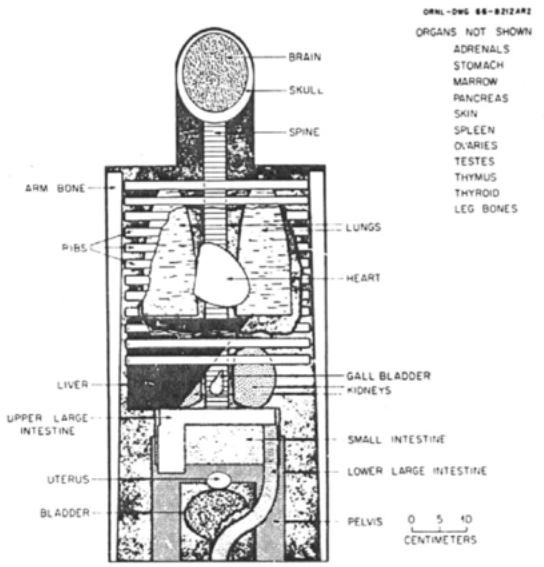

Figure 4.3: Anterior view od the principal organs in the head and trunk of the adult phantom developed by Synder et al. Adapted from [2].

Modifications to MIRD phantom including new equations for new geometries, tabulated absorbed fractions of monoenergetic photons and electrons and tabulated radionuclide S-values, able to use in radiation protection, radionuclide therapy and medical imaging were developed. These modifications allow the use of stylized phantoms by National and International Corporation in order to establish guidelines and regulations related to industrial and medical use of ionising radiation [2].

4.2.2.2 Voxel Phantoms (1980s-Present)

With the introduction of imaging techniques as CT and MRI, 3D visualisation of the internal structures of the body and image storage was possible and a new era of phantoms began: the voxel phantoms generation.

Three different types of tomographic images as CT and MR images of live subjects and cross-sectional cadavers images are the basis of a voxel phantom.

The basis unit of these phantoms is the voxel, the 3D representation of a pixel, represented as a tiny cube with a volume of the pixel size multiplied by the slice thickness.

A tomographic phantom is created by following the next steps: (1) acquisition of a set of medical images, that are (2) subsequently segmented and classified into different organs or tissues of interest. Then, (3) density and tissue composition have to be specified for each label representing the segmented organs. Finally, (4) the segmented images slices are registered into a 3D volume and the implemented computational phantom can be used with MC modelling simulation tools, for organ doses calculations and for a given clinical X-ray diagnostic protocol [19, 2].

The ICRP reference phantoms were conceived based on CT image datasets of individuals close to the reference man and woman (height and weight). After segmentation the body height is adjusted to the reference valued by scaling the voxel size and the organs masses are adjusted by mathematical operations such as voxels addition and subtraction. At the beginning these phantoms were associated to a large slice thickness which limited the definition of small organs and reported skin and walled organs with small holes.

The number of voxel phantoms available are still increasing over the years, and the standard ones are REGINA and REX, two ICRP reference adult phantoms , created from CT images of a Caucasian female patient of 43 years, and of a Caucasian 38-year-old male leukaemia patient, respectively [2, 19].

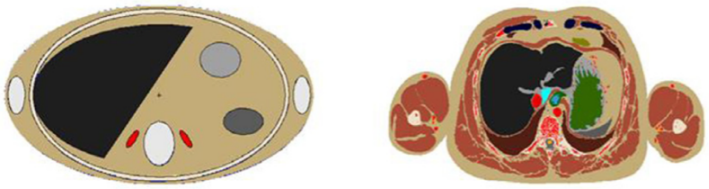

Figure 4.4: Comparison of stylized adult phantom (left) and VIP-Man phantom (right).Adapted from [2].

As can be seen in Figure 4, voxel phantoms have a more realistic representation of the internal organs, however, the construction a whole-body phantom, using images of live subjects, faces several challenges. One of the challenges is the fact that to create a whole-body phantom, images slices of the entire body are needed which, due to excessive radiation exposure, are not carried out in a routine medical examination. Also, for a more accurate representation of the human body, a large amount of internal organs and tissues have to be identified and segmented, which is

a time-consuming and a difficult process [2].

4.2.2.3 BREP Phantoms (2000s-Present)

The BREP phantoms based on polymesh surfaces and NURBS technology arose from the need to simulate organ motions as cardiac and respiratory motion in order to understand and 'predict' the effects of respiration on radiation treatment.

NURBS technology is a mathematical model used in computer graphics to generate and represent curves and surfaces [2]. Using quadratic and superquadratic surfaces, BREP phantoms are much more flexible since tools operations such as extrusion, drafting or shelling are available, which enables inclusion of complex anatomic features [1].

NCAT phantom, one of the first phantoms of the third generation, was built from the CT image dataset of the VIP and from gated MRI datasets to extend 3D anatomy to 4D.

In 2000s, Xu predicted the advantages of a 'hybrid' phantom that combines voxel and BREP-type of surface geometries, in order to obtain a new generation of models that 'should be realistic enough to accurately represent major radiosensitive tissues and organs, and flexible enough to represent different populations' [2]. In fact, the Vanderbilt group led by Michael Stabin reported a 'family' of adult and paediatric phantoms using ICRP-89 reference body and organs values to adjust NURBS surfaces. This approach proved to be beneficial since NURBS-based phantoms can be developed more quickly than using voxel and manually segmentation, the phantoms have a higher level of internal consistency and the problem of missing organs is avoided [53].

BREP phantoms have demonstrated the feasibility to develop models that represent a wider range of individuals in terms of body weight and height as well as organ motion [2].

Chapter 5

Segmentation Methods

Image segmentation is the step that precedes image analysis since it influences the description, recognition or classification of an image or its constituents [26]. The aim of segmentation is to subdivide an image into constituent parts, objects or regions of interest (ROIs) that have similar grey levels, texture or colour [54].

The division of an image is based on detection of two properties of the pixels in relation to their local neighbourhood: discontinuity and similarity. While discontinuity translates abrupt variations of grey level and detects edges, methods based on similarity detect homogeneous parts according to a pre-specified criterion and are region based techniques [26].

After segmentation, the different segments can be separated from the background, measured and quantified. Therefore, image segmentation has several applications: as in machine vision, biometric measurements or medical imaging. In diagnostic field, segmentation is an essential tool that enables the clinicians to examine the characteristics of a suspicious region and decide if it exhibits signs related to a particular disease or anomalies such as micro-calcifications in mammograms [26, 55].

Due to the complexity of the human body, for a more accurate segmentation, different methods have to be combined. Along this chapter, some methods used in previous studies to segment organs in CT examinations of thorax and abdomen will be presented, together with techniques that were used in this work: thresholding and region growing are described.

5.1 Segmentation Methods for thorax organs

In a CT examination of thorax and abdomen, several organs, as spinal canal, trachea, lungs, breast, heart, thoracic aorta, spleen, liver and kidneys, are affected by ionizing radiation. For this reason, their segmentation is relevant for diagnosis and radiotherapy planning [56, 57].

Segmentation of anatomic objects is more challenging when compared to segmentation of geometrical objects, due to the large variability in size, position, shape and composition of human organs. Besides anatomic features of the organs, artefacts that can arise from CT scanner as partial-volume artefacts, metal artefacts or steak artefacts result of peristalsis, respiratory, cardiac and patient motion limit the outcome quality of segmentation [58].

The use of medical images of an anthropomorphic phantom instead of CT images of human patients reduces and eliminates the appearance of artefacts due to patient motion. However, difficulties related to the lack of organ tissue homogeneity in shape within and among different slices are independent of the patient or phantom [58]. In the literature different approaches categorized as model fitting, image registration and rule-based systems can be found. Model fitting approaches aim to adapt a parametric model of a part of the anatomy to image data [56]. Shani and others developed one of the earliest model-driven approaches that is considered as a grand departure from data-driven techniques such as thresholding. Since major organs have familiar shapes and are positioned in predictable places in the body, Shane aimed to identify organs in medical images by using three-dimensional geometric primitives called generalized cylinders as models of the shape of organs [59].

On the other hand, image registration based approaches use a priori information about organ morphology from reference images to extract different organs. An example is the method proposed by Bae [60] to extract liver structure in CT images. A reference image in which the liver occupies almost the entire right half of the abdomen cross section is chosen by a user, then segmentation is performed sequentially slice-by-slice. The abdomen is extracted from the background using grey-level thresholds and liver is isolated by evaluating the boundary of globally connected regions in the threshold image of the ROI.

In rule-based systems, relations between anatomic objects are formulated by facts, and the task of detecting or visualizing anatomic object is guided by rules as reported by Archip [61].

Besides the methods above mentioned, lately, approaches based on the use of

artificial neural networks (ANNs) have gained interest. ANNs are computed systems inspired by the biological neural networks designed to simulate the way in which the human brain process information. An ANN is formed from a huge number of nodes connected with different weights (or coefficients), and is trained and optimized by a learning process [62].

Lee and Chung [63] proposed a method based on shape analysis, image contextual constraint and relationship between slices. A multimodule contextual neural network, that uses the grey level and contextual information supported by neighbouring pixels, is adopted to segment each image slice into disconnected regions. Knowledge of abdominal anatomy and the overlapping information between adjacent slices provided by descriptors and fuzzy variables are used during the recognition process to identify the same in different slices.

Despite of the poor results, Koss came up with a valid principle: the combination of textures and an artificial neural network to segment abdominal organs. Texture, defined by Webster as *"the visual or tactile surface characteristics and appearance of something"*, may help on objects recognition and distinction. Statistical texture analysis derives a set of statistics from the distribution of pixel values or blocks of pixel values. While first-order statistics are calculated from the histogram formed by the grey-scale value of each pixel and include mean, standard deviation, range, entropy and the q^{th} moment about the mean, second-order statistics takes the spatial distribution of the grey-scale distribution into account. This are based on pair of pixels and are known as Haralick transform. According to Koss, these various statistics are fed into a Hopfield Neural Network to perform the segmentation [64].

The approach studied in this work, is based on the literature and its results above described. The properties of the pixels, discontinuity and similarity, are the basis of the algorithms used: a thresholding and a region growing algorithm.

5.1.1 Thresholding Method

Thresholding based image segmentation aims to divide an input multilevel image, $f(x,y)$, into a binary image, $g(x,y)$. The division is achieved by individually comparison of pixel values with the value of a predefined threshold, T. If a pixel has intensity greater than the threshold, the pixel is assigned with 1 or 255, on the other hand, pixels with intensity lower than T, compose another class and are assigned with 0, Equation 5.1 [57, 54]. This approach is beneficial in cases of images with light objects on gloomy surroundings and requires minimal complexity of computation. However, it has limitation, in case of images without clear peaks of intensity

or in images with similar grey levels.

$$g(x,y) = \begin{cases} 0 & if \quad f(x,y) < T \\ 1 & if \quad f(x,y) \geq T \end{cases} \tag{5.1}$$

The selection of the proper value T may be done based on the valleys in the histogram of the image, or from priori knowledge of the grey levels of the objects of interest [26]. If the selection of threshold fails, over or under-segmentation of the image may occur, i.e., the segmented region might be smaller or larger than the ROI [54].

According to Haas, thresholding approaches can be used in medical images as a pre-segmentation process to define body outline and to extract bone equivalent and lung equivalent tissue due their large inherent grey level difference when compared to the surrounding tissue. Therefore, the first step is definition of the body outline using the HU range from -175 to 750. Then, since bones have higher density, bones segments can be extracted using a range 145 to 1000. On other hand, lungs are mainly composed by air, their density is lower and, consequently, have lower HU values. Lungs are extracted within the outline of body segments using the HU range -1000 to -195 [56].

5.1.2 Region Growing Algorithm

Region growing can be categorized as a region-based and as a pixel-based image segmentation method since it involves the selection of an initial seed point and relies on pixels similarity to grow uniform regions [54]. With this approach, an initial seed point is chosen, then, the region grows by aggregation of pixels that fulfil a certain homogeneity criterion. The simplest property used is pixel's intensity, a pixel is appended to a region if the difference between the gray level of a neighbour pixel and the average intensity of the region is lower than a tolerance level pre-defined, Equation 5.2 [26]

$$|f(x,y) - \mu_{R_c}| \leq T \tag{5.2}$$

In Equation 5.2, $f(x,y)$ represents the neighbour pixel and μ_{R_c} is the mean grey level of the region that is growing at its current stage R_c and is calculated from:

$$\mu_{R_c} = \frac{1}{N_c} \sum_{(x,y)\epsilon R_c} \sum f(x,y), \tag{5.3}$$

where N_c is the number of pixels contained in R_c [26]. The mean grey level of a region is used as a criteria to determine whether a neighbouring pixel should be included or not to minimise the dependence of the region on the seed pixel selected. Indeed, as can be observed in Figure 5.1, if instead of using the average value of the region, the intensity of seed is used, the region selected might differ.

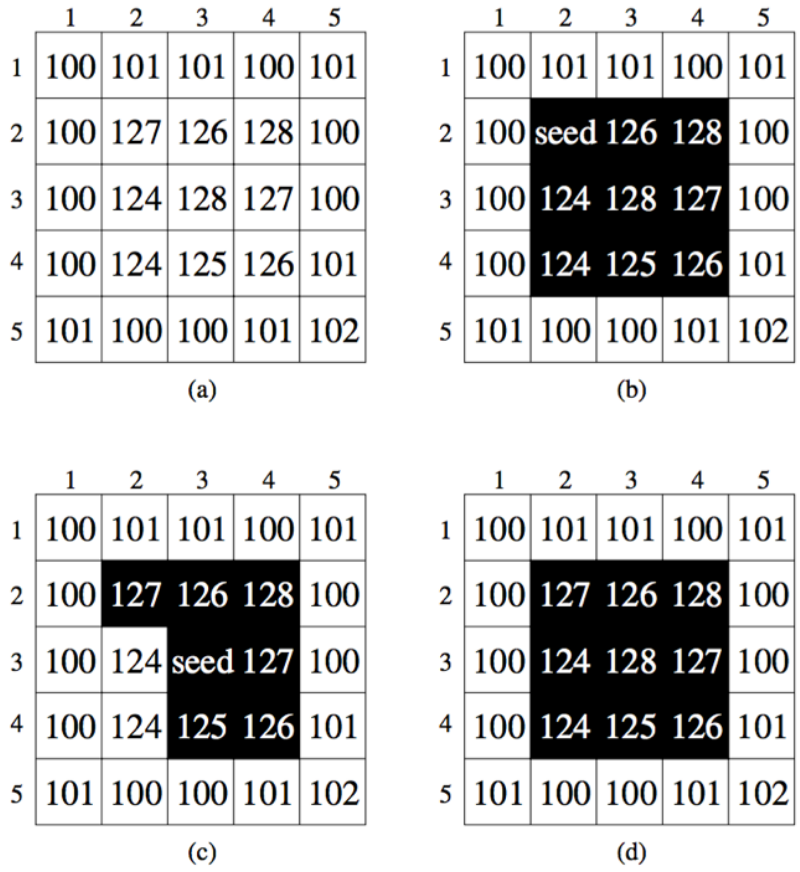

Figure 5.1: Example of performance of a region growing algorithm using different seed pixels and a additive tolerance criteria (T=3). (a) Original image. (b) The result with the seed pixel at (2,2. (c) The result with seed pixel at (3,3). (d) The result of region growing using any seed pixel within the highlighted region and the mean grey level. Adapted from [26].

Grey level texture or colour and distance between pixels might be used instead of pixel intensity as a criterion of region growing [54].This method has several advantages, is a simple approach that can correctly separate regions with similar properties, its criteria and initial point can be chosen in order to have better results, and it is a noise resistant method [54]. In this study, a region growing algorithm was used to extract organs with similar grey levels, as liver, spleen, aorta, heart, breast and kidney.

Chapter 6

Materials and Methods

As described in Chapter 4, to develop a computational voxel phantom several steps need to be followed: (1) acquisition of CT medical images in Paediatric Hospital of Coimbra Hospital and University Centre using a Siemens SOMATOM Definition scanner of 64 slices; (2) identification and segmentation of organs of interest and finally, (3) creation of the voxel phantom and performance of MC simulations for phantom validation.

Along this chapter, a description of the materials and the applied methodology in the different phases is described. Section 6.1 is related to the data acquisition. The features of the CT system and of the anthropomorphic phantom used to acquire the medical images are described. The IC used to directly measure dose are also presented in this section.

The approach followed to extract the different radiosensitive organs is described in Section 6.2. Several metrics as accuracy, sensitivity, specificity, false positive rate (FPR), Hammoude distance and Jaccard Index were used to evaluate segmentation, and their description can be also found on Section 6.2.

The phantom validation was accomplished through MC simulations performed using PENELOPE code. Furthermore, the basic concepts of MC simulations, the computer code system PENELOPE and the structure of PenEasy, an extension of PENELOPE used for dose calculations and image acquisitions, are summarised in Section 6.3.

MC simulations were also used for evaluation of image quality and to determine the difference signal-to-noise ratio (SDNR) of different images when lung calcifications are taken into account. The methodology is described in Section 6.4.

6.1 Phase 1 - Data Acquisition

6.1.1 CT system

The images were acquired in the Paediatric Hospital of Coimbra and University Centre using a Siemens SOMATOM Definition scanner of 64 slices.

According to the manufacturer, this unit is equipped with Fully Assisting Scanner Technologies (FAST) Combined Applications to Reduce Exposure (CARE) and CARE kV technology that adjusts the voltage and the current as low as possible without compromising the contrast-to-noise ratio (CNR) and the image quality, minimising the patient dose [65]. Due to this technology, this equipment has the flexibility to perform several examinations as cerebral, spinal, cardiac, thorax CT, volume perfusion and trauma studies. The gantry has dimensions of $198 \times 238 \times 93cm$, an aperture of $78cm$ and the detector's thickness is 19.2 mm which provides a reconstruction matrix of 512×512 pixels.

As aforementioned, the acquisition mode used involves CARE kV which sets the appropriated voltage according to the exam and the organ imaged. For this study, two different adult protocols were tested, a routine chest protocol and a HRCT protocol. HRCT is more sensitive and specific than normal chest CT, therefore, has become an essential tool for evaluation of pulmonary diseases. While, routine protocols are considered exams of low dose, that need contrast, HRCT uses narrow collimation and high spatial frequency reconstruction algorithms to assess lung parenchyma.

The acquisition range was set manually from last cervical vertebra (C7) until intervertebral space L1 and L2. Images were reconstructed by FPB algorithm using modulation of tube current, $72/148mA.s$ and tube voltage, $100kV$ (CARE dose 4D and CARE kV).

6.1.2 Phantoms

In this study, two types of phantoms were used. Firstly, an anthropomorphic phantom was used for image acquisition. Then, a PMMA cylinder phantom was used for system validation Figure 6.2(b). The cylinder phantom made of polymethyl methacrylate with dimensions of 320×150 mm, has five holes with a diameter of 12.6 mm, one located at the centre and other four positioned 90^{o} apart and 10 mm from the edge. The phantom is placed with its long axis perpendicular to the plane of the transverse CT scanner and an ion chamber is placed in the different holes to

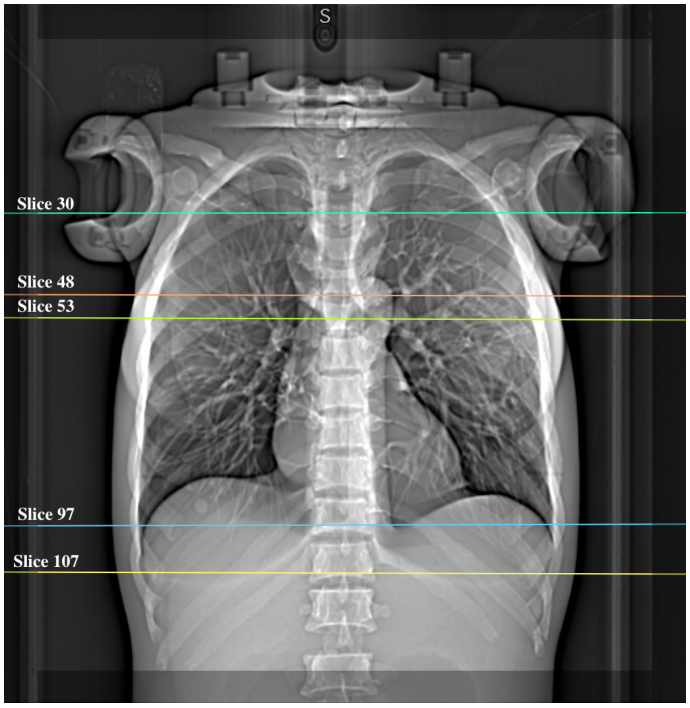

Figure 6.1: Topogram of the Kyoto PBU-60 acquired in the Paediatric Hospital of Coimbra Hospital and University Centre using a Siemens SOMATOM Definition scanner of 64 slices.

measure $CTDI_{100}$ at the centre and at the periphery [66], Figure 6.7(b)

The anthropomorphic phantom, Kyoto PBU-60, is a life-size human phantom with a life-size synthetic skeleton, used in CT and conventional radiography to help optimising scanning conditions. The organs of Kyoto PBU-60 are composed by materials with radiology absorption and Hounsfield numbers similar to human body [51].

The phantom can be disassembled into 10 different parts, however for this study only the trunk part that includes organs such as lungs, trachea, liver, spleen, aorta, among others, was used. While synthetic bones are made of epoxy base resin, soft tissue and organs are composed of urethane base resin (SZ-50) that has in its composition hydrogen, carbon, nitrogen and oxygen [51].

Since breast is considered one of the most radiosensitive organs, two breast implants from Polytech Health & Aesthetic [67] were used to simulate breast. To understand and study the influence of breast size in organ dose, two implants with different sizes were chosen. According to the manufacturer, these implants are filled with a cohesive, non-liquid silicone gel, and have anatomically shape of the breast [67].

The implants were attached to the phantom with adhesive as showed in Figure

6.2(a).

(a) (b)

Figure 6.2: Physical phantoms used in this study: (a) Acquisition set-up of the anthropomorphic phantom measurements, Kyoto PBU-60. Breast implants are also showed.(b) PMMA cylinder phantom used to measure $CTDI_{100}$.

6.1.3 Ionisation Chamber (IC)

An IC is a device used in dosimetry to detect radiation and consists of a certain volume filled with gas between two electrodes connected to a high voltage supply. When an IC is exposed to an X-ray beam, ions pairs are produced from interactions between the X-rays and the volume of gas. Due to the voltage applied, ions are accelerated and attached to the electrodes creating a measurable current [68].

In this study, a RaySafe Solo CT detector with an active length of 100 mm and an active volume filled with air of 3 cm^3 was used for two different measurements: free-air kerma and $CTDI_{100}$ [69].

The pencil chamber measures the integral of a single rotation dose profile thus, the measured value, also called the 'meter reading' has to be converted into $CTDI_{100}$

using Equation 6.1.

$$CTDI_{100} = \frac{f(mGy/mGy).meterreading(mGy).l(mm)}{N.T(mm)}, \tag{6.1}$$

where f is a conversion factor that takes into account the material of acquisition, l is chamber's length, 100 mm and NT is the beam width, 38.4 mm (64 detectors with an aperture of 0.6 mm). f assumes a value of 0.9 mGy/mGy in Lucite and 1.0 mGy/mGy in air [36].

6.2 Phase 2 - Image Segmentation

After data acquisition, the medical images were imported to OsiriX Lite version 8.5, an image processing application that allows visualisation and processing of images in format DICOM (Digital Imaging and Communications in Medicine) [70].

Software tools such as OSIRIX are fundamental since they enable visualisation of the slices of each clinical protocol, and allow information extraction about the localisation, position and shape of the different radiosensitive organs.

Image processing and segmentation was performed using Matlab R2016b software [71]. Firstly, images were imported to Matlab and ordered using specific commands for DICOM images format, *dicomread.m* and *dicominfo.m*.

6.2.1 Organs Extraction

As mentioned in Section 5.1, previous studies reported that spinal canal, trachea, lungs, breast, heart, aorta, liver and kidneys are the most radiosensitive organs compromised in a thorax and abdomen CT examination [56] [57].

The approach used to segment the different organs combine two different segmentations methods: a threshold algorithm and a region growing algorithm. In 2008, Haas reported the importance of a presegmentation to detect body outline and to detect bones and air/lung equivalent tissue.

6.2.1.1 Threshold methods – Pre-segmentation

Thresholds methods, the simplest and easiest segmentation methods, are based on a threshold value and convert an image into a binary image. The threshold value is chosen according to the valleys of the histogram of the image or is setting by the user. In this study, instead of using just a value, different ranges of HU values were

defined to, first, detect the body outline, then to segment lung tissue and large air cavities and finally to extract bone tissue.

The ranges of HU values were defined based on information provided by the histogram of slice n34 and information reported by Haas [56]. Slice 34 and its histogram was used, since it incorporates different radiosensitive organs of interest: breast, lung and bones.

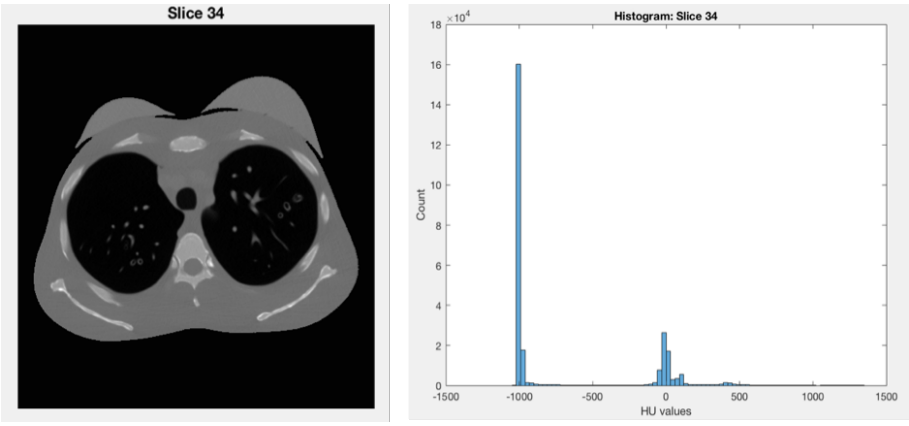

Figure 6.3: Tomographic image with mediastinum window(a) and its corresponding histogram (b).

According to the histogram, (Figure 6.3)(b), pixels may take values between, approximately, -1000 and 2000, and three peaks can be distinguished, one around -1000, another around 0 and one at, approximately, 450 HU. Knowing that lower values correspond to segments with lower densities and are matched with black, the peak around -1000 represents the air of the background and the air equivalent tissues as lungs and trachea. On the other hand, the peak associated with higher HU values corresponds to brighter or white segments, the bones.

The first step of pre-segmentation was extraction of the body from the background. Since the pixels of background have the lowest CT numbers (assigned with black), the body region was defined as the pixels with intensities between -100 and 750 HU. Segments areas smaller than the body area were discarded, since they might correspond to artefacts or objects without interest (e.g. Patient's table).

Within the body outline, air cavities (lung, trachea and bronchus) are extracted using the HU range -1000 to -600. To differentiate the different organs the images reconstructed with lung parenchyma window, Figure 6.3(a)) were used. Pulmonary window is more appropriate to visualise air cavities and allows definition of lungs as the major group of pixels within the range previous stated, while trachea and bronchi corresponds to the second one. The area of pixels group was measured using features of the *bwconncomp.m* function that find connect components in a binary

image.

Finally, bones segments can be extracted within the body outline applying the HU range between 160 and 1000.

Figure 6.4: Reconstruction of a tomograpraphic image in lung parenchyma window.

6.2.1.2 Region Growing Algorithm

While bone and air cavities have HU values that present large differences, soft tissues, assigned with different grey levels, have similar pixel's values. Since threshold methods might give inaccurate results, an approach using region growing algorithm was followed to extract breast, liver, spleen, kidney, heart, venae cava and aorta.

Firstly, a 2D region growing algorithm was implemented to test segmentation in individual slices, then the algorithm was adapted to 3D. As described in Section 5.1.2, region growing algorithms evaluate the intensity of an initial seed point given and compare it with the value of neighbours pixels. The major difference between the 2D and the 3D algorithms is the number of adjacent pixels in each iteration. While in the first algorithm, 8 pixels are evaluated, in 3D algorithms the number increases to 26, Figure 6.5 [72].

To avoid segmentation errors, the segmentation process of soft tissues is not fully automatic, in fact, initial conditions as position of the initial point (slice index, x and y), tolerance and localisation of the organ of interest (indexes of the initial and final slices) are defined by the user and vary from organ to organ. In some cases, due to organs irregularities in shape and in anatomy position, i.e., anatomy position differs from one slice to another, multiple initial points are considered (e.g. heart).

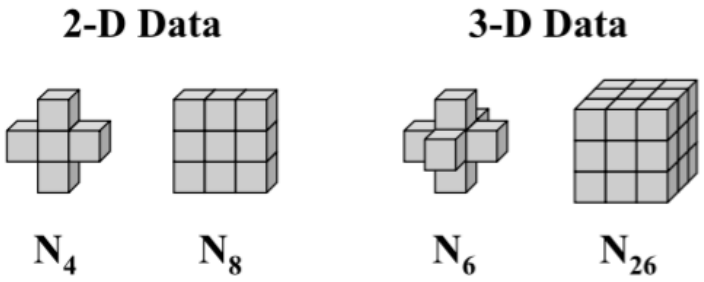

Figure 6.5: Neighborhoods for 2D and 3D implementations [72].

The initial conditions are summed up in the following table, and were chosen using OsiriX.

Table 6.1: Initial conditions for the region growing segmentation algorithm

Organ		Tolerance (HU values)	Initial Seed Points (x,y)	Slice Index
Breast	Left	20	(89,362);(139,359);(170,376)	40
	Right	20	(100,141)	36
Liver		18	(205,154)	112
Spleen		18	(228,380)	112
Kidney		13	(278,354)	112
Heart		18	(218,228);(224,284);(276,288)	40
Venae Cava		13	(232,244)	90
Aorta		16	(279,284)	59

6.2.2 Segmentation Evaluation

Segmentation might be a time consuming and difficult process, however, is a fundamental step on the development of computational voxel phantoms. In fact, the accuracy of organ dose estimations relies on segmentation performance and on its ability to discriminate and segment the different organs.

Therefore, evaluation of the performance of the segmentation algorithms is indispensable and an important subject. Besides that, evaluation allows comparison between different segmentation methods and selection among two or more possible segmentations.

Evaluation methods can be divided into three categories: analytical methods, empirical "goodness" methods and empirical discrepancy methods. Analytical methods evaluate the performance of algorithms by analysing their principles and properties.

While empirical "goodness" methods judge the quality of segmented images by computing goodness measures, empirical discrepancy methods compare the segmented image against a segmented reference image often called as ground truth [73].

The ground truth images are obtained by a manual segmentation of the original image and can be seen as the correct/ideal segmented image. Empirical discrepancy methods are the most common ones and evaluates the discrepancy between two images in terms of the number of regions, and their localisation, size and statistics of the segmented regions, in case of a region-based methods. In boundary-based approaches, discrepancy is measured by evaluating the location and shape accuracies of the extracted region boundaries in [73].

Discrepancy can be measured by different parameters or metrics and determines how far the actually segmented image is from the ground truth [74].

In this work, the reference images were manually segmented using the program ImageJ and different metrics were tested.

ImageJ is a Java image processing program used to display, edit, analyse, process and save images of different format like TIFF, GIF, JPEG, BMP, DICOM, FITS and "raw" [75]. Regardless all the transformations, adjustments and measures that can be performed by ImageJ, this program was used since it can read image sequences and allow definition of different ROIs that can be later recognised by Matlab.

6.2.2.1 Ground Truth Masks

To generate the segmented reference images, 5 images out of the 112 slices were chosen. Since the organs segmented are not imaging in all the slices, was decided that each organ should be represented in at least 2 of the 5 slices chosen. Besides this criteria, the five slices might be distributed along the examination range, i.e., they might not be adjacent. In this way, the slices 30, 48, 53, 97 and 107 were chosen.

The different organs presented in each slices were segmented using the polygon function and ROI manager. To read and to compute a binary mask of the different ROIs created with ImageJ, different fucntions of Matlab were used.

In this approach, each ground truth image is a binary mask of an organ that is compared to the mask created by the segmentation algorithms. In total, 27 reference masks were created from the 5 slices. Different parameters were calculated in order to measure the discrepancy between the masks.

6.2.2.2 Confusion Matrix - Accuracy, Sensitivity, Specificity and False Positive Rate (FPR)

Image segmentation can be considered as a pixel classification process. If an image consists of N pixel classes, a confusion matrix C of dimensions N can be constructed, where each entry C_{ij} represents the number of pixels in the class j classified as class i by the segmentation algorithms. In this case, the result of segmentation is an image of two classes, a pixel is assigned with 1 or 0 whether it belongs or not to the mask [74]. The corresponding confusion matrix is:

Table 6.2: Example of a confusion matrix C of 2 dimensions.

		Predicted	
		Negative (0)	Positive (1)
Actual	Negative (0)	TN	FP
	Positive (1)	FN	TP

TN stands for true negative, and represents the number of pixels assigned in 0 in both masks, FN or false negative is the number of pixels misclassified as 0. On the other side, false positive, FP, represents the pixels classified as organ by the segmentation algorithm that are part of the background assigned with 0, in the ground truth mask. Finally, TP or true positive corresponds to the organ pixels in both masks.

Different evaluation parameters can be calculated out of the confusion matrix: accuracy, sensitivity, specificity and FPR [76]. Accuracy (AC) translates the proportion of the total number of predictions that were correct and is determined using the following equation:

$$AC = \frac{TP + TN}{TP + FP + FN + TN} \tag{6.2}$$

Sensitivity also called recall or true positive rate is calculated as the number of correct positive predictions divided by the total number of positives.

$$Sensitivity = \frac{TP}{TP + FN} \tag{6.3}$$

Specificity or true negative rate evaluates the number of negative cases that were correctly identified and is calculated by Equation 6.4:

$$Specifity = \frac{TN}{TN + FP} \tag{6.4}$$

FPR also known as the false alarm ration refers to the number of negative cases incorrectly classified as positive.

$$FPR = \frac{FP}{TN + FP} \tag{6.5}$$

6.2.2.3 Hammoude Distance

The Hammoude distance, H, is a standard metric that does not favour under-segmentation and over-segmentation used to compare and evaluate the similarity between a segmented image and a reference one.

The similarity is measured by comparing the number of common and non-common pixels in the two segmentations results. If X and Y correspond to the ground truth mask and to the binary segmented image, respectively, Hammounde metric is given by Equation 6.6, where # represents the number of pixels.

$$H = \frac{\#(X \cup Y) - \#(X \cap Y)}{\#(X \cup Y)} \tag{6.6}$$

Hammoude metric can also be expressed using true/false positives/negatives, i.e., based on confusion matrix [77]:

$$H = \frac{FN + FP}{TP + FN + FP} \tag{6.7}$$

Hammoude distance has values between 0 and 1, a value of 1 stands when there is no intersection between segmentations and the value of 0 when the two segmentations are equal. The inverted Hammoude index is used to evaluate discrepancy and is calculated using the following equation [78]:

$$H' = 1 - H \tag{6.8}$$

6.2.2.4 Jaccard Index

Jaccard index or Jaccard coefficient (J) is an external index of cluster validity, that access the degree to which two classifications of data, in this cases, segmented masks agree. The coefficient is calculated by inspecting the labels assigned to all pairs of pixels in the image, or in other words, is defined as the size of the intersection divided by the size of the union of the images, Equation 6.9 [74]:

$$J = \frac{\#(X \cap Y)}{\#(X \cup Y)} = \frac{\#(X \cap Y)}{\#(X) + \#(Y)\#(X \cap Y)} \tag{6.9}$$

Jaccard index values varies between 0 and 1, a value of 1 corresponds to a perfect segmentation.

6.2.3 Conversion of HU to density values

Segmentation methods were performed based on CT numbers, since each pixel has a HU value associated. Nonetheless in voxel phantoms, voxels are assigned with a specific label which corresponds to a density value.

The HU value of each voxel can be converted, through a calibration curve, to the electronic density of the tissue within the voxel. The calibration curve is defined based on four types of tissues: air, lung, tissue, bone and their respectively density and CT numbers range [79, 80].

Table 6.3: CT numbers and density range for the four materials used in the ramp for converting CT numbers. Adapted from [79]

Organ	Hounsfield Number	Density (gcm^{-3})
Air	0-50	0.0001-0.044
Lung	50-300	0.044-0.302
Tissue	300-1125	0.302-1.101
Bone	1125-3000	1.101-2.088

While the HU range used in the calibration curve is from 0 to 3000, in the CT images used the range was from -1024 to 1997. Hence, firstly it was necessary to transform the HU range of the CT images to the range required, using Equation 6.10:

$$HU_{transformed} = (HU + 1024) \times (\frac{3000}{3021}) \tag{6.10}$$

For each organ or tissue, the average HU value was computed and the corresponding density value was obtained via linear interpolation of the values set at the boundaries of the Hounsfield numbers bins. Origin 7.5 is data analysis software produced by OriginLab Corporation that includes curve-fitting, peak analysis and signal processing, and was used to interpolate the density values [81].

6.2.4 Phantom Definition

The Fortran routine *readPhantom.f95* was used to create the files necessary for simulation and visualisation of the voxel phantom. The use of this routine requires two input files: the *phantomfile.dat* and the *organlist.dat*. While, the first can be

in binary or ASCII format and is the matrix resultant of segmentation, where each pixel corresponds to an organ label, the second is create by the user and lists every organ, and the corresponding material and density that the phantom possesses, in the following order: OrganID, MaterialID and density.

```
anaritamonteiro@ubuntu:~/Desktop/Phantom_Rita$ ./readPhantom.exe
  Please insert the name of the phantom file (max 20 characters).
Rita.dat
  Is your file in binary or in ASCCI? (type 0 for bin or 1 for ASCII)
1
  Type in the number of voxels of the phantom in x,y,z.
512, 512, 112
  Type in the voxel resolution in x,y,z /cm.
0.06348, 0.06348, 0.3
  Type in the number of different materials in the phantom.
12
  Type in the number of organ IDs - number of lines in organlist.dat.
12

 >>> Characteristics of your phantom file:
 > Number of voxels in x,y,z:  512  512  112
 > Voxel resolution in x,y,z /cm:  0.0634800   0.0634800   0.3000000
 > Phantom size (approximate value) in x,y,z /cm:    32.5017586    32.5017586
 33.6000023
 > Total number of voxels:  29360128

  Please check if these values are correct. Do you wish to continue? (y/n)
  Please type y or n.
```

Figure 6.6: Instructions of the Fortran routine *readPhantom.f95* used to create the voxel phantom.

Figure 6.6, shows the instructions provided by the readPhantom.f95 routine when it is executed. The user should follow the instructions and type the number of voxels of the phantom in x, y and z direction, the voxel resolution in each direction, and the total number of materials and organ IDs in the phantom.

Six different files are created by this routine: *phantom.ct*, *phantom.vox*, *organlistAsRead.dat*, *ct-den-matXY.dat*, *ct-den-matXZ.dat*, *ct-den-matYZ.dat*. The *.vox* file is required for simulations and has a 7 line header that provides information (number of voxels in each direction and the corresponding resolution) about the phantom. The *organlistAsRead.dat* is a verification file of the *organlist.dat* file created by the user. Finally, the last three files are visualisation files that allow visualisation of the phantom in x,y and z planes. Each ct-den-matXY/XZ/YX.mat file has a corresponding GNUplot file, visualiseVoxelsDensityXY/XZ/YZ.gpl that enables the visualisation of the phantom slice per slice.

6.3 Phase 3 - Monte Carlo Simulations

Due to the random nature of interactions of radiation with matter, MC methods which are based on the principles of probability theory and statics, are commonly

used to simulate the stochastic nature of the interaction of ionising radiation with matter [82].

In MC simulations, the individually track of the trajectory of each simulated particle is named as history and can be defined as the random sequence of free flights of particle that terminates when the particle suffers an interaction causing its absorption, its energy decreased or after multiple scattering interactions [82, 83]. Each interaction mechanism has to be characterised in terms of its corresponding differential cross section, which determines the distribution of probabilities of the random variables, such as the mean free path between successive interactions events, type of interaction, loss of energy and angular deflection of each particle, energy and direction of the generated secondary particles and the final states of the interactions [83].

The number of histories simulated can be adjusted for a minor statistical uncertainty and in order to obtain more reliable results with increase of computational time. However, nowadays, with the introduction of powerful computer processors and reasonable memory storage, the implementation of MC simulations in various computational physics areas is easier and represents an essential tool.

Nowadays, the number of MC codes available to simulate radiation transport has increased. Among several MC codes, some of the most used in simulation of electrons and photons are ETRAN, ESG4 and PENELOPE. MCNP/MCNPX, GEANT4 and FLUKA can be also used to track neutrons and heavy charged particles [83].

A detailed description of PENELOPE code will be given in the following sections, since it was used in this study.

6.3.1 PENELOPE

PENELOPE code stands for PENtration Energy Loss Of Positrons and Electrons which performs MC simulations of electrons, photons and positrons transport in arbitrary material systems limited by quadratic surfaces in the energy range from 50 eV to 1 GeV [46, 82]

The PENELOPE source file consists of subroutines written in FORTRAN code, a database that contains information for creating material cross-section files, and three mains programs (penmain, pencil and penslab) which differ in terms of geometry description. The Fortran subroutines are organized in five source files: the *penelope.f*, the basic package for transport simulation, the *pengeom.f* which allows particles simulations through quadratic geometries, the *penvared.f* that contains rou-

tines for variance reduction, the *timer.f* based on timing subroutines and *material.f* which is the main program to generate material data file. [46, 82]

Coupled to PENELOPE another general-purpose main program was used, named PenEasy which peculiarity is the possible definition of voxelized geometries that can be combined with quadratics geometries. For this work, the PenEasy program was also used to produce 2D images projections.

6.3.2 PenEasy

PenEasy (version 2015-05-30, compatible with PENELOPE 2014) is a general-purpose main program for the PENELOPE MC system also coded in FORTRAN language. Its algorithm was structured in a way that a particle track is generated and followed until it suffers an interaction with the medium (a "knock" where it loses energy, changes its direction and in certain cases, produces secondary particles).

Computationally the algorithm consists of calling repeatedly the subroutines JUMP that calculates the distance to the next interaction event, STEP which determines if an interface is crossed before completing the step and KNOCK that simulates an interaction event and its effect in the particle energy loss and direction of movement [82].

A simulation can be interrupted through four different ways: (1) if the number of total histories defined by the user at the beginning of simulation has been completed, (2) if the statistical uncertainty for a certain tally, also previous defined by the user, is reached, (3) if the allotted time has been exhausted or (4) if the user itself uses a "stop" command [46].

PenEasy operates form the input file which is divided in the following sections:

- **General simulation settings:** in this section details on the simulation configuration such as the total number of histories to simulate, the allotted time (real time or CPU time), number of initial seeds and update interval are defined.
- **Source description:** PenEasy allows the user to choose between two types of source models: source box isotropic gauss spectrum or source phase space file if initial particles state is read from an external phase space file. For the purpose of this work, only the first was active and used. Therefore, in this section, the user defines the type of particles, position of the source, its direction and semi-angular beam aperture and the values of spectral energy.
- **Geometrical section (section PENGEOM+PENVOX):** as afore-

mentioned PenEasy allows different type of geometries: quadratic geometries, voxelized geometries or a combination of both. In the quadratics files, saved with .geo extension, the bodies that can be defined by quadratic volumes such as the detectors or calcifications, are defined. A body is defined by quadratic surfaces, the index value of side pointer (-1 or +1 depending if the geometry is inside or outside the surface) and the label of the material that composes it. On the other hand, the phantoms are defined in the voxel files, with extension .vox, where the number of pixels in the x, y and z direction are defined as the resolution in each direction. Each voxel is identified with the material label that composes it and the corresponding density value. When quadratic and voxelized geometries are combined, the user has to define the quadratic transparent material.

- **Description of each body's material and transport parameters:** in this section the materials that are listed in the geometries files (quadratic and voxel) and the transport simulation parameters are defined in ascending order. The material files can be created by the user though the application available in PENELOPE code (material.exe). In this application, two different ways can be used to generate the material file: manual introduction of fundamental information about the material as chemical composition, density and mean excitation energy; introducing an index number associated with PENELOPE's database that contains 280 pre-defined materials. The simulation transport parameters are [82]:
    - **EABS** – defines the cutoff energy, or in another words, the maximum value of energy for a given particle before it is locally absorbed.
    - **C1** – corresponds to the average angular deflection produced by multiple elastic scattering between two consecutive elastic events.
    - **C2** – represents the maximum average of energy loss between two consecutive elastic events.
    - **WCC** – is the cutoff energy loss for hard inelastic collision.
    - **WCR** – defines the cutoff energy loss for hard bremsstrahlung emission.
- **Tally sections** – PenEasy has several tallies available, however, according to the purpose of the simulations only some of them are turned ON. In this work, only two type of tallies were used, the tally pixelated imaging

detector to obtain the simulated images and the tally energy deposition to estimate the absorbed dose in each material. For each tally, specific parameters and a relative statistical uncertainty has to be set by the user.

6.3.2.1 Tally pixelated imaging detector

To generate an image of the simulated configuration system, the user has to turn on the pixelated imaging detector tally in the input file and has to specify several parameters. Firstly, is necessary to identify the material of the detector according to the one defined in the geometry file in the section PENGEOM+PENVOX and the type of photons that reach the detector and can be detected (primary photons and scattered photons).

Therefore, different images can be obtained according to the type of filter of photons and to the detection mode chosen. Three possible detection modes are available: (1) energy integrating where the image signal is, for each pixel, the energy deposited (eV) per unit pixel area (cm^2) per simulated history, (2) photon counting if the image signal is the number of photons that deposits an amount of energy that exceeds the threshold pre-defined per unit pixel area per simulated history and, finally, (3) the photon energy discriminating mode where a full pulse height spectra is tallied for each pixel.

6.3.2.2 Tally energy deposition

The tally energy deposition allows evaluation of dose in the different materials or organs, since it reports the total energy deposited in each material and its unit is in electron-volt per history.

Since the values of dose are usually given in mGy, the values reported in the tally energy deposition, given in $eV/hist$, must be converted. Besides that, in order to simulate quantities such as $CTDI_{100}$ a conversion factor (CF), which is an in-air normalisation method based on pencil-chamber exposure readings for a single axial scan taken at the scanner isocenter as shown in Figure 6.7(a), is required. This CF has been previously described [84, 85, 86] and is defined as a function of the beam energy E and the beam collimation NT by the following equation:

$$CF_{E,NT} = \frac{(CTDI_{100,air,measuredper110mAs})_{E,NT}}{(CTDI_{100,air,simulatedperparticle})_{E,NT}}, \tag{6.11}$$

where the nominator has units of $mGy/(110mAs)$ and is measured in air at the centre of the CT gantry, and the denominator, in units of $eV/particle$, is the result of

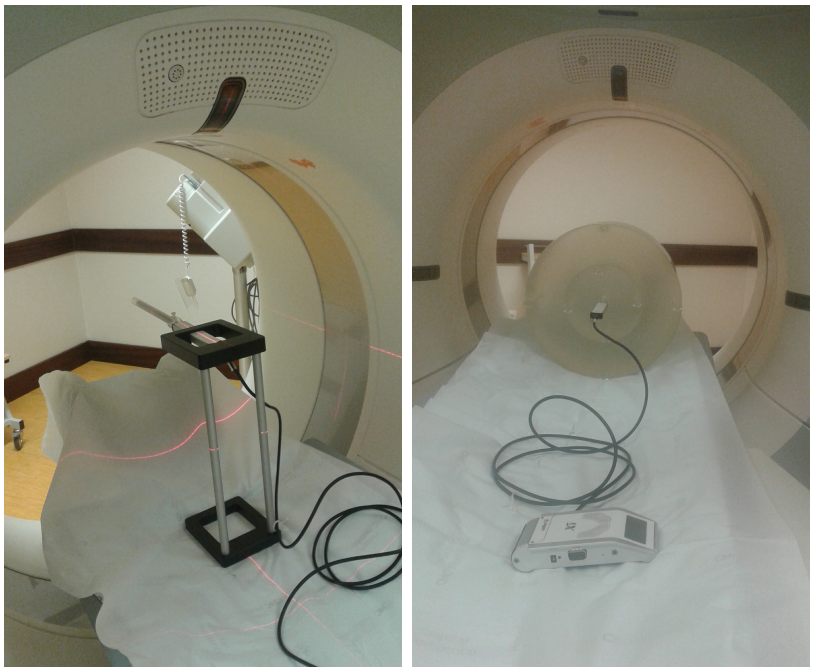

(a) (b)

Figure 6.7: Experimental configurations (a) To measure air kerma free in air. (b) To measure $CTDI_{100,centre}$ using a PMMA phantom and an IC.

simulating the IC under the same conditions of the free-in-air measurements. Thus, the absorbed dose in $mGy/110mAs$ for an organ or tissue is

$$D_{per110mAs} = D_{simulated} \times CF \times N, \tag{6.12}$$

where N is the number of x-ray rotations, in this case, since it is a single axial scan N equals 1.

On the other hand, to evaluate organ doses the conversion is based on the definition of electron-volt and Gray. An electron-volt corresponds to the amount of energy an electron gains after being accelerated by one volt ($1eV = 1.602 \times 10^{-19} J$), an $1Gy$ equals to $1J/kg$, therefore, the energy deposition value is converted into mGy with the following equation:

$$D(mGy) = \frac{E(\frac{eV}{part}) \times 1.602 \times 10^{-19} J}{M_{mat} \times 1000} \times N_{part}, \tag{6.13}$$

where $M_{mat}(kg)$ is the mass of a given material in kilograms and N_{part} is the total number of particles.

Table 6.4: List of the components and their properties used in MC simulations.

Component	Dimensions (cm)	Material	Density (gcm^{-3})
Detector	$40.0 \times 1.92 \times 50.0$	Gadolinium Oxysulfide	7.440
IC (outer shell)	$r = 0.63$, $h = 10.0$	PMMA	1.190
IC (interior)	$r = 0.309$, $h = 10.0$	Air	0.001
Phantom PMMA	$r = 16.0$, $h = 15.0$	PMMA	1.190
Patient Table	$37.5 \times 2.0 \times 50.0$	Carbon	2.000
Calcifications	$r = 0.3$, $r = 0.7$, $r = 1.5$	Calcium Phosphate	3.180

6.3.3 Definition of geometries and materials

Several geometries and materials were defined for the purpose of this work. Materials that constitute the different organs of the phantom and the calcification were created using the *material.exe* aforementioned. The fundamental information as chemical composition and density of each material was manually inserted based on information provided by ICRP [87] (see Appendix A).

In Table 6.4, the components that were designed for the simulations, description of their dimensions, material type and density are reported. The material files of the PMMA phantom, IC, detector and patient table were generated through the material files available in the database of PENELOPE code.

6.3.4 Energy Spectrum

In this study two types of X-ray spectrum were considered in the MC simulations: a polychromatic spectra for simulations involving the IC, anthropomorphic organs phantom and the PMMA phantom and several monochromatic spectrum for calculation of the SNR.

The spectral data for the first simulations was obtained trough the X-ray spectra simulation tool available online on the website of Siemens [88]. Based on algorithms developed by Boone et al. [89], in this application it is possible to select the peak tube voltage in a range of 30 to 140 kVp with 1kVp steps, can choose different filter's material and their thickness and normalise the value for the air kerma (set as 1 mGy by default).

According to Boone, these spectral data has an uncertainty in photon fluence and spatial and energy distribution, of approximately 10-15%.

To evaluate the SNR and find its maximum for imaging of lung calcifications with different sizes, several simulations were run using as input source several monochromatic spectra between 30 kVp and 120 kVp [46, 89].

6.4 Evaluation of image quality

In X-ray diagnostic, the ability to view small details is related to image quality which can be improved by applying higher voltages and, consequently, higher doses. Due to the risk of radiation exposure, parameters for examination should be chosen according to the ALARA principle. Therefore, dose optimisation which involves a compromise between radiation dose and image quality has become a concern for the physics community [90].

In this work, image quality assessed by SDNR was studied in order to estimate the most suitable energy to detect a calcification in the lung.

In image quality assessment, image signal and image noise are important parameters and depend on the number of incident photons. While the image signal can be related to the number of detected photons, image noise corresponds to the pixel's stochastic fluctuation around their mean value, in other words, image signal corresponds to the average HU value, S, of an image or ROI and image noise corresponds to the standard deviation (σ) [91]. The detectability of an object, in this case a calcification, can be measured using SDNR based on these parameters and is described by the following equation:

$$SDNR = \frac{S_B - S_O}{\sigma_B}, \tag{6.14}$$

where S_B corresponds to the signal of the background, S_O to the signal of the object of interest and σ_B is the standard deviation of the noise in the background [91]. In this work, ImageJ was used to measure the different quantities.

Chapter 7

Results and Discussion

This chapter aims to present and analyse the results obtained in the different phases of this study. First, in Section 7.1, the performance of the segmentation approach is discussed. For a better understanding of the segmentation process, the results of manual segmentation and the results of organs extraction for a particular slice are presented.

Section 7.2 presents the phantom validation by comparing the organs mass and density of the voxel phantom created with the recommended values for a Female Adult Reference Phantom provided by ICRP.

Besides phantom validation, the MC model implemented was validated using measured and simulated values for $CTDI_w$ and $CTDI_{100}$. These results are also discussed in Section 7.2.

Lastly, Section 7.3 summarises the results of the simulations with different monochromatic X-ray spectrum in order to evaluate image quality and to find the optimal X-ray energy that maximises the SDNR for a lung calcification.

7.1 Evaluation of Segmentation

Figure 7.1(b), is a result of the manual segmentation performed using ImageJ software and illustrates the potential of the described segmentation approach on slice 48, i.e., segmentation of bone, lung, trachea, breast, heart and aorta.

The ROI of each organ previous mentioned was converted to a binary mask named ground truth mask which was compared to the segmented mask. While Figure 7.1(c) illustrates the overlapping of the different ground truth masks, Figure

7.2 shows the different masks that result from the segmentation algorithm.

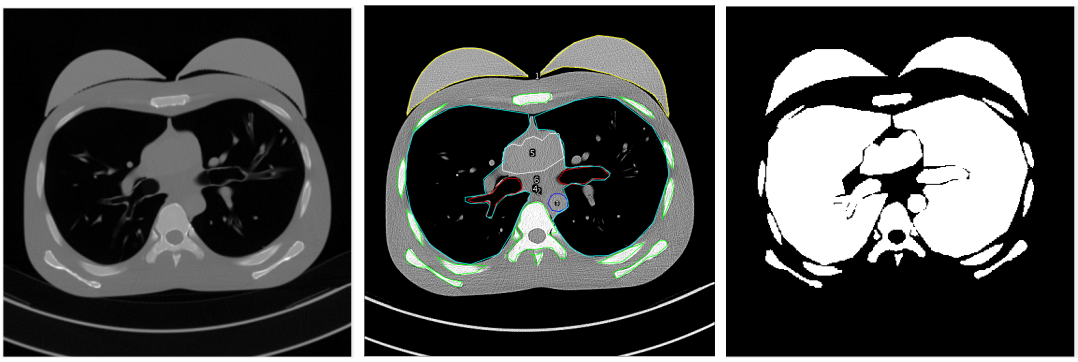

(a) (b) (c)

Figure 7.1: Example of Chest CT protocol, with lung parenchyma window, above the bronchial bifurcation. (a) Original Image. (b) Results of manual segmentation. (c) Ground Truth Mask.

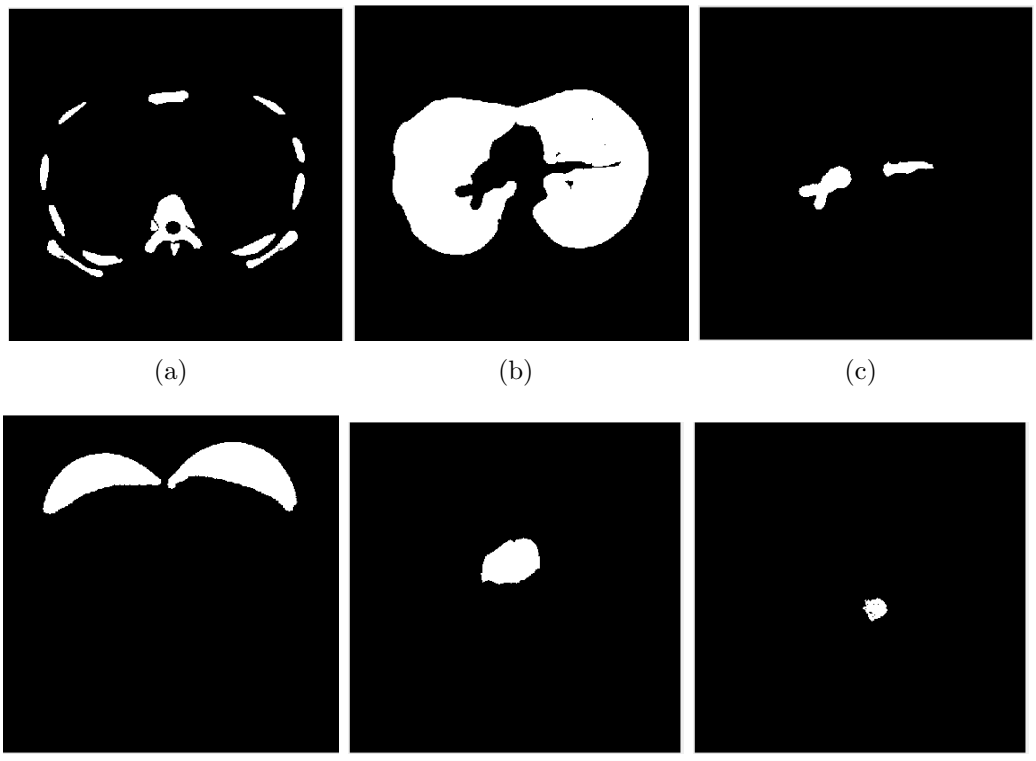

(a) (b) (c)

(d) (e) (f)

Figure 7.2: Results of extraction of the different organs imaged in slice 48: (a) bone, (b) lungs, (c) bronchi, (d) breast, (e) heart and (f) aorta.

The quality of detection is reported in Table 7.1. Based on Table 7.1, is possible to conclude that for every organs the accuracy is higher than 0.95, which means a

correct segmentation in at least 95% of the pixels. The conclusions over the accuracy value need to be supported by the values of specificity, sensitivity, and FPR since these metrics may reflect over fitting (in cases of values equal to 1). In this case, to avoid misinterpretations, the Jaccard Index and the Hammoude Distance were also evaluated. While higher values of Jaccard Index are directly related with a more accurate segmentation, the lower the Hammoude distance, the better is the segmentation.

Table 7.1: Performance of segmentation algorithm in Slice 48. Accuracy, sensitivity, specificy, FPR, H: Hammoude Distance and J: Jaccard Index.

Organ	Accuracy	Sensitivity	Specificity	FPR	H	J
Bone	0.9933	0.9978	0.9931	0.0069	0.1550	0.8450
Lung	0.9667	0.9905	0.9584	0.0416	0.1150	0.8850
Bronchi	0.9883	0.9678	0.9894	0.0106	0.2020	0.7980
Breast	0.9788	0.9925	0.9774	0.0226	0.1917	0.8083
Heart	0.9856	0.9856	0.9891	0.0109	0.1780	0.8220
Aorta	0.9960	0.9960	0.9922	0.0078	0.1655	0.8345

Table 7.2: Overall performance of segmentation algorithm. Accuracy, sensitivity, specificy, FPR, H: Hammoude Distance and J: Jaccard Index.

Organ	Accuracy	Sensitivity	Specificity	FPR	H	J
Bone	0.9943	0.9993	0.9941	0.0059	0.1522	0.8478
Lung	0.9756	0.9963	0.9692	0.0308	0.1428	0.8572
Trachae&Bronchi	0.9914	0.9780	0.9920	0.0080	0.1597	0.8403
Breast	0.9818	0.9773	0.9820	0.0180	0.1878	0.8122
Heart	0.9891	0.9815	0.9896	0.0104	0.1591	0.8409
Aorta	0.9933	0.9925	0.9933	0.0067	0.1729	0.8271
Venae Cava	0.9933	0.9445	0.9945	0.0055	0.2152	0.7848
Liver	0.9800	0.9900	0.9896	0.0104	0.1591	0.8409
Spleen	0.9924	0.9989	0.9921	0.0079	0.1554	0.8446
Kidney	0.9909	0.9924	0.9908	0.0092	0.2715	0.7285

The metrics summarised in table 7.2 evaluate segmentation results of five different slices (Slice 30, 48, 53, 97 and 107). These results are consistent with the results displayed in Table 7.1, where the accuracy is higher than 95% for every segmented organ. This confidence level is supported by low values of FPR, which discards over fitting and may justify a good detection of boundaries. Boundaries can be characterised by abruptly changes in image intensity which in region growing algorithms is controlled by the tolerance level. Thus, the values of FRP are, in these case, a good indicator of the tolerance levels pre-defined in Table 6.1.

The values of Hammoude distance and Jaccard Index reveal some inaccuracies and problems in segmentation, mainly in extraction of kidney (J = 0.7285) and venae cava (J = 0.7848). In fact, segmentation of kidney, venae cava and trachea was an arduous process. Since the range acquisition was from vertebra C7 to the intervertebral space L1-L2, the kidney is only scanned in the last seven slices, consequently, kidney is not imaged in its totally. Therefore, its irregular shape and the small discrepancy range existent between the HU values of the kidney and the HU values of the background contribute for a difficult boundary detection and consequently to a less accurate segmentation. On the other side, the imprecisions in segmentation of trachea and venae cava can be explained by the simillarity of intensities between these organs and adjacent organs (lung and liver, respectively) which might led. in some slices, to a incorrect classification. To improve extraction of trachea, the bronchi bifurcation was found in order to detect the right and left bronchi individually [56]

The tolerance levels and the others initial conditions were adjusted in order to obtain a satisfactory segmentation and acceptable values as the ones presented.

7.2 Phantom Validation

The results in this section are subdivided into two different subsections. As mentioned in Chapter 3, the interaction of radiation with matter and the deposition of energy is influenced by the material density, Thus, the density and mass of the segmented organs was evaluated by comparison with recommended values.

To support validation, results of MC simulations were compared with values measured with the same acquisition conditions.

7.2.1 Determination of masses and densities of the organs

Figure 7.3 represents the calibration curve used to determine the densities of the different organs. As aforementioned, the curve was based on values pre-defined in previous studies [79, 80]. In total 250 points were interpolated from the curve, and a correspondence was established between the points interpolated and the calculated mean HU value of each organ. The densities found for each segmented organ were compared with the densities established by ICRP for the Adult Reference Phantom which are summarised in Table 7.3.

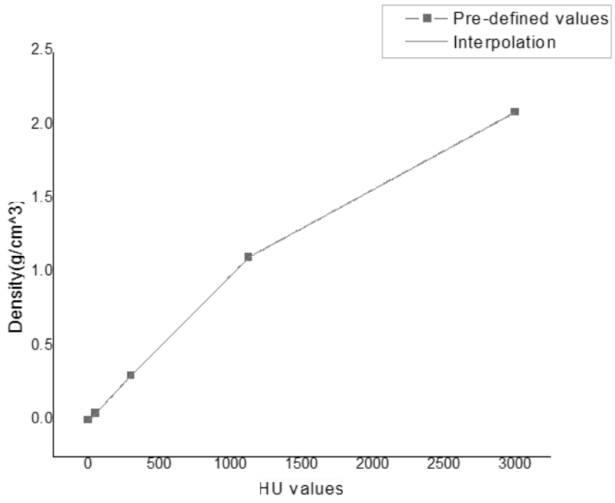

Figure 7.3: Calibration curve used to interpolate the density of the organs.

The relative difference between results is calculated using the following formula:

$$RelativeDiference = \frac{value_{measured} - value_{simulated}}{value_{simulated}} \times 100\% \tag{7.1}$$

Table 7.3: Organ and tissue masses for the phantom created and for the Female Adult Reference Phantom [87].

Organ	HU	$Density_{interpolated}$ (gcm^{-3})	$Density_{ICRP}$ (gcm^{-3})	Relative Difference (%)
Bone	1378.48	1.234	1.136	-8.617
Lung	174.61	0.173	0.385	55.166
Liver	1079.57	1.057	1.050	-0.617
Spleen	1057.61	1.036	1.040	0.409
Kidney	1017.96	0.970	1.010	4.002
Breast	989.70	0.970	1.020	4.906
Trachae&Bronchi	227.79	0.227	1.030	77.914
Heart	1041.34	1.020	1.050	2.861
Venae Cava	1035.66	1.014	1.030	1.507
Aorta	1041.04	1.019	1.030	1.002
Tissue	966.13	0.942	1.000	5.826

According to Table 7.3, the relative difference between the density interpolated and the values recommended by ICRP is lower than 5% in 7 out of the 11 segmented organs or tissues (58.3%), and smaller than 10% in 9 organs which corresponds to a percentage of 75%.

Despite of the approach used in this study have been reported as an acceptable

and accurate method to determine density values [80], the discrepancy (relative difference higher than 50%), between the interpolated and the established values for lung and trachea reveal some controversies.

Comparing the mean HU value achieved for lung (174.61) and, consequently, the density value (0.173 gcm^{-3}) with the values established for the calibration curve 6.3, is conclude that the values are within the values range established, 50 to 300 for HU values and 0.044 to 0.302 gcm^{-3} for density. However, the lung density defined by ICRP (0.385 gcm^{-3}) for an adult reference phantom is not in agreement with the values range, and consequently with the value achieved.

On the other side, the discrepancy related with the values of trachea (77.914%) is explained by trachea anatomy. Trachea is composed of C-shaped cartilaginous rings linked longitudinally by annular ligaments of fibrous and connective tissue [92]. Radiographically, the anatomy of trachea is demonstrated by the tracheal air space [93], consequently, trachea is associated with CT numbers in the same range of CT numbers of lung which does not reflect trachea anatomy. Thus, for a more realistic determination of trachea density, using this approach, the mean HU value should be calculated by discarding the voxels that correspond to the air column and as a consequence, by taking into account just the voxels corresponding to the cartilaginous rings.

Since small differences in densities can be dosimetrically significant, the density values of lung and trachea were adjusted to the density recommended by ICRP110 [87], while for the other organs the interpolated value is accepted.

Besides the comparison of the density, the mass of the organs phantom was also compared to the organs masses recommended by ICRP110. The masses were calculated using the relationship between density, mass and volume (see Equation 7.2). Volume was estimated by multiplying the number of voxels that composes an organ with the volume of a single voxel ($0.063 \times 0.063 \times 0.300cm$).

$$\rho = \frac{M}{V} \tag{7.2}$$

In order to understand and discuss the discrepancies between results, is important to keep in mind that the ICRP recommended masses correspond to the average masses of an adult reference phantom which may not coincide with the masses of the organs of the anthropomorphic phantom used.

The lowest relative difference for organs mass was achieved for spleen, which also corresponds to the lowest discrepancy in density. This support the results obtained in Table 7.2 for spleen segmentation. On the other hand, regarding the

Table 7.4: Volume, masses and the recommended values of the different radiosensitive organs.

Organs	N_{voxels}	Volume (cm^3)	$Mass_{calculated}$ (g)	$Mass_{interpolated}$ (g)	Relative Difference (%)
Bone	1138466	1376.16	1780.54	-	-
Lung	3965737	4793.71	806.16	848.52	4.99
Liver	816868	987.42	1043.68	1400.00	25.45
Spleen	104908	126.81	131.34	130.00	-1.03
Kidney	19733	23.85	24.10	-	-
Breast	482815	583.62	575.69	500.00	-15.14
Trachae	41207	49.81	11.33	7.99	-41.82
Heart	473296	572.11	589.72	620.00	4.88
Venae Cava	21585	26.09	26.874	-	-
Aorta	46103	55.73	57.40	-	-
Tissue	6277726	7588.40	7588.40	-	-

results presented, the highest discrepancy between masses was obtained for trachea, followed by liver and breast.

The relative difference of -15.14% for breast is explained by the fact that the implants used to simulate breast have significantly different sizes, and consequently different masses which does not correspond to a reference and normal situation.

On the other side, the variation of the mass of trachea is explained by the segmentation approach. As known from trachea anatomy, trachea at the Carina bifurcates into the right and the left main stem bronchi [92], however, for the purpose of this study and to facilitate segmentation, the left and the right bronchus were not distinguished. In fact, their segmentation was coupled to trachea. Thus, the mass value achieved for trachea, $11.33g$, corresponds to the mass of trachea and to the mass of the left and right main bronchus, while the mass reported by ICRP corresponds just to trachea.

7.2.2 System Validation

As mentioned in Section 6.3.2.2 two sets of measurements using an IC free-in-air were performed in order to validate the MC model. While the first set of measurements was made using only the IC, the second set of measurements was taken using the IC and the CTDI phantom. The conditions of acquisition were similar for both measurements: the IC was exposed to an x-ray beam of 120 kVp, 38.4 mm ($64 \times 0.6mm$) of thickness and a tube current of 110 mAs. All the measurements

were taken during a single axial rotation of the CT scanner and were converted to CTDI using Equation 6.1. The measurements, in the first case, were taken with the IC placed at the isocentre of the gantry, while, for the second sets, measurements were obtained at the centre and at two of the four peripheral (0º and 90º) insert positions of the CTDI phantom. Analogous simulations were then performed. The geometry of the CTDI phantom used in MC simulations is illustrated in Figure 7.4(a). Figure 7.4(b) shows the simulation geometry along the z axis where the IC is inserted at the centre position of the phantom.

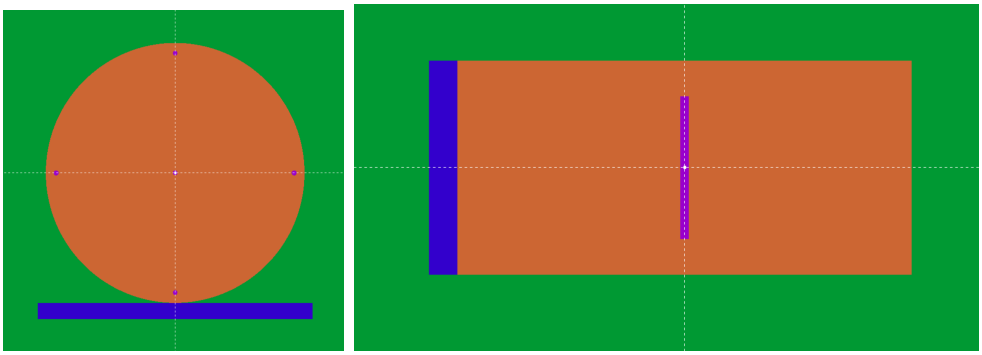

(a) (b)

Figure 7.4: Geometries used in MC simulations. (a) Frontal view of the CTDI phantom. (b) Longitudinal view of the IC inserted at the center of the CTDI phantom.

The values measured and simulated of $CTDI_{100}$ in air and the corresponding CF are displayed in Table 7.5.

Table 7.5: Conversion factor to get the Monte Carlo simulations results from eV/g per source particle to mGy.

E_{Total} $(eV/particle)$	$CTDI_{100,simulated}$ $(eV/g/particle)$	$CTDI_{100,measured}$ $(mGy/110mAs)$	CF $(mGy.g.particle/(110mAs.eV))$
0.51	170.79	11.31	0.0662

In order to simulate a single rotation of the source, MC simulations were performed with the source at different positions. Therefore, for each configuration, four MC simulations were implemented, with the source positioned at 0º, 90º, 180º and 270º. The total energy deposited results from an interpolation of 36 points of the simulations values. Figure 7.5, represents the variation of the amount of energy deposited per particle in a single axial rotation.

As illustrated in Figure 7.5, for a source angle of 180º, the energy per particle decreases almost 50%. In this position, the X-ray photons passes trough the patient

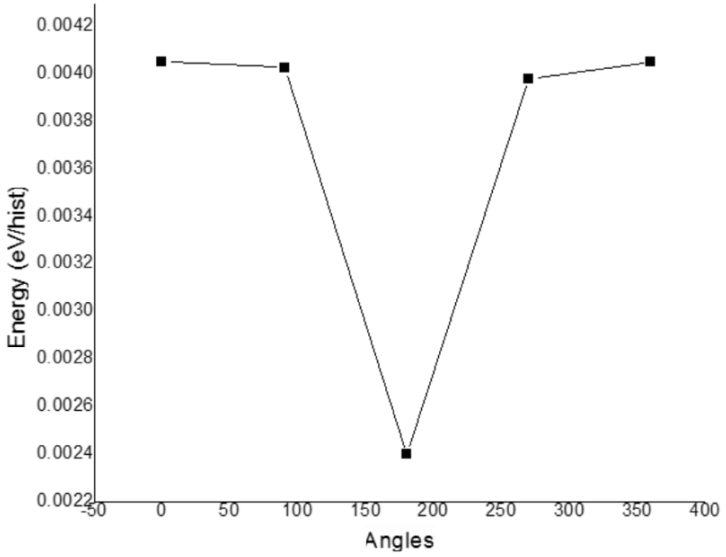

Figure 7.5: Energy deposited in the IC positioned at the centre of the CTDI phantom in function of source position.

table before reach the IC, part of their energy is lost in interaction with the electrons of the material, which demonstrates the influence of the patient table on $CTDI_{100}$.

Table 7.6: Comparison of measured and simulated $CTDI_{100}$ results from a single axial scan in the three considered positions of the CTDI body phantom.

	Tally (eV/hist)	$CTDI_{100,simulated}$ (mGy)	Reading (mGy)	$CTDI_{100,measured}$ (mGy)	Relative Difference (%)
Center	0.131	2.882 ± 0.086	1.786	4.185 ± 0.209	31.124
0º	0.427	9.415 ± 0.282	3.598	8.433 ± 0.422	-11.649
90º	0.372	8.219 ± 0.247	3.432	8.044 ± 0.402	-2.177

Table 7.6 summarises the measured and simulated values of $CTDI_{100}$. The uncertainties of the simulations are related to the uncertainty of the spectral data used, about 10-15 % [89], and to the statistical uncertainty of each simulation. The number of histories for each simulation was defined at 3×10^{12} to achieve statistical uncertainties of approximately 3%. Therefore, the overall uncertainty for simulated values is approximately 15 %. The experimental results have an uncertainty of 5 % which corresponds to the uncertainty of the IC.

The highest difference between the results from experimental measurements and from calculations was observed when the IC was inserted in the hole at the centre of the phantom (31.124%). This result could be justified by the absence of a

beam-shaping filter, also defined as bow-tie filter in the simulation geometry. In CT scanners two filters can be distinguished: a flat filter, mostly made of aluminium, and a bow-tie filter made of metal or/and plastic. While the flat filter aims to remove the low-energy photons from the X-ray spectra (included in the X-ray spectra used in this work for simulation), the primary function of a bow-tie filter is to homogenise the photon flux at the detectors by attenuating the fan beam, mainly, at its periphery [94]. Due to the use of bow-tie filters, less attenuation is expected by peripheral regions [94]. Therefore, simulation of a bow-tie filter that modulates the output of a radiation source could have a non-negligible impact on the dose distributions inside the phantom [95].

The lowest difference (-2.177 %) was achieved for the measurements of the hole at 90º.

The simulated value for CTDI weighted has a relative difference of 0.87% when compared to the value measured (see Table 7.7). Regarding the decrease of deviation between experimental and calculated values, different initial conditions of MC simulations, such as spectral data, distance between source and detector, and material of patient table, were tested. At the end, the optimal initial conditions were set to an X-ray spectra of 120 kVp with an aluminium filter of 6.8 mm normalised for an air kerma of 4mGy and a distance source-IC of 54 cm.

Considering the results previous discussed and the uncertainty associated with simulations around 15%, the initial conditions aforementioned were kept constant for the following simulations.

Table 7.7: Comparison of measured and simulated $CTDI_w$.

$CTDI_{w,simulated}$ (mGy)	$CTDI_{w,measured}$ (mGy)	Relative Difference (%)
6.827 ± 0.205	6.887 ± 0.344	0.870

7.2.3 MC simulations for phantom validation

Apart from the MC simulations performed to evaluate the computational model implemented, a MC simulation, with a similar geometry to the one represented in Figure 7.6, was executed to evaluate $CTDI_{100}$ and the performance of the voxel phantom created. Table 7.8 displays the results from experimental measurements and from calculations.

The IC chamber has an active volume filled with air of $3cm^3$. The low density of the air ($1.00 \times 10^{-3} gcm^{-3}$) in comparison with the density of the organs of the

Figure 7.6: Experimental configurations to measure $CTDI_{100}$ using the Kyoto PBU-60 and the IC.

Table 7.8: Experimental and simulated results for $CTDI_{100}$ using the IC and the Kyoto phantom.

Tally (eV)	$CTDI_{100,simulated}$ (mGy)	Reading (mGy)	$CTDI_{100,measured}$ (mGy)	Relative Difference (%)
0.661	14.589 ± 0.437	6.518	16.973 ± 0.849	13.813

phantom makes photon interactions less frequent [94]. Consequently, in order to obtain statistical errors of about 3%, MC calculations would be very time consuming.

Therefore, the statistical uncertainty considered was 3%, which is the statistical uncertainty of MC simulations for $CTDI_{100}$ in air, described in Section 7.2.2.

A relative difference of 13.813 % was achieved between the results from experimental measurements and from calculations, which considering the simulations uncertainties and the absence of the bow-tie filter, represents a good agreement between the simulated and measured values and validates the implemented phantom.

7.2.4 Estimation of organ doses

After phantom validation through simulations of $CTDI_{100}$, the organ doses were estimated for a single axial rotation of the source. The results displayed on Table 7.9 were determined using Equation 6.11 and organs masses defined in Table 7.4 and are given in terms of the tube current used in data acquisition (110 mAs).

Table 7.9: Estimation of the organ doses for a single axial scan.

Organ	Tally (eV/hist)	D (mGy/110mAs)
Bone	1.464E+05	5.435
Lung	7.574E+04	6.210
Liver	4.609E+03	0.292
Spleen	5.430E+02	0.273
Kidneys	6.979E+01	0.191
Trachea	1.935E+03	11.308
Heart	3.530E+04	3.956
Aorta&VenaeCava	3.029E+03	2.375

To estimate organ doses, the voxel phantom was exposed to a rectangular beam of photons with 39 *mm* of thickness. The distance source-phantom was 54 cm and the source was placed at a distance of 15 cm in z direction. Due to the source position, the target organs were trachea and lungs, which corresponds to the highest doses, 11.308 mGy and 6.210 mGy, respectively. On the other side, the doses in liver, 0.292 mGy, spleen, 0.273 mGy and kidneys 0.191 mGy are minimal significant and, mainly due to scattered radiation, since these organs are not directly irradiated.

These results validate the use of the voxel phantom to estimate organ doses in hospital environment for different CT protocols.

7.3 Determination of SDNR

As described in Section 6.4, the SDNR was evaluated in order to find the optimal energy that maximises dose optimisation. PenEasy program was used to simulate the exposition of the voxel phantom created to monochromatic X-ray beams with different energies (range from 30 keV to 120 keV). The total absorbed dose in lungs were evaluated through the tally energy deposition, while tally pixelated imaging detector provided information to produce 2D images projections which enables cal-

culation of signal and noise. In Figure 7.7, the curve of lung dose are presented. In all the results the uncertainty of MC simulations was smaller than 1%.

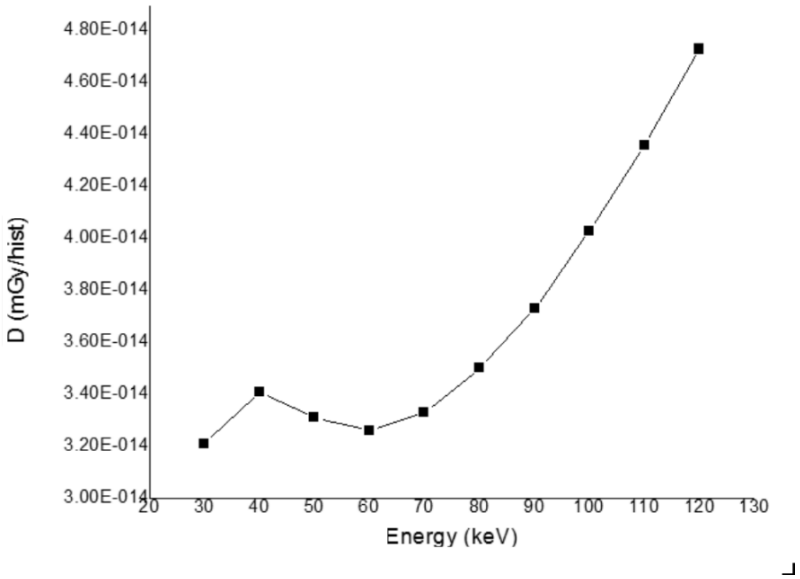

Figure 7.7: Dose deposited per particle in the lungs for each monoenergetic energy.

The value of the energy deposited per particle (eV/hist) in the lung was provided by the tally energy deposition, this value was converted to joules and then divided by the mass of the organ (see Table 7.4) in order to evaluate the dose. As expected, the dose tends to increase as energy increases.

According to the literature, several studies have been reported in order to evaluate the performance of two different CT protocols for evaluation of localised lung lesions [96, 97]. These studies compare image quality and radiation dose between a low dose CT protocol and a standard dose. The difference between these protocols is the tube current, while in the low-dose CT protocol the tube current is kept at 50 mAs, in a standard dose CT protocol, its increased to 150 mAs. The tube voltage peak, 120 kVp is the same for both protocols. The studies reveal, that the ability of diagnosis and lesion detection is approximately the same for both, however the radiation dose is minimised for lower tube currents [96, 97]. In addition, information provided by Siemens shows that the tube peak voltage in HRCT protocols, used for lungs examinations, is 120 kVp [98].

Tube peak voltage affects the X-ray spectra and is related to the mean energy of photons [99]. In MC simulations, monochromatic X-rays beams were used, however, in CT examinations, the X-ray beam is polychromatic. Using the tool provided by Siemens [88], is possible to calculate an X-ray spectra of 120 kVp, Figure 7.9.

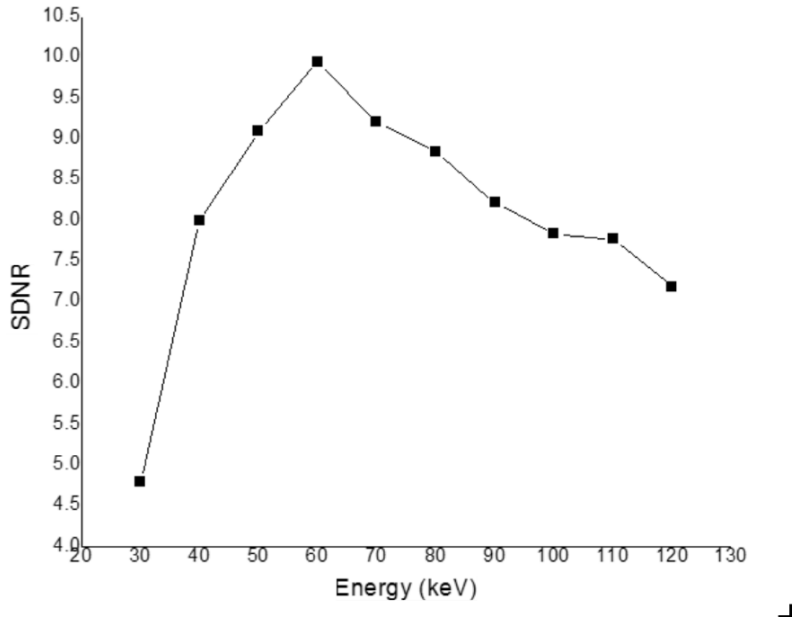

Figure 7.8: SDNR results obtained by MC simulations for a lung microcalcification of 7mm.

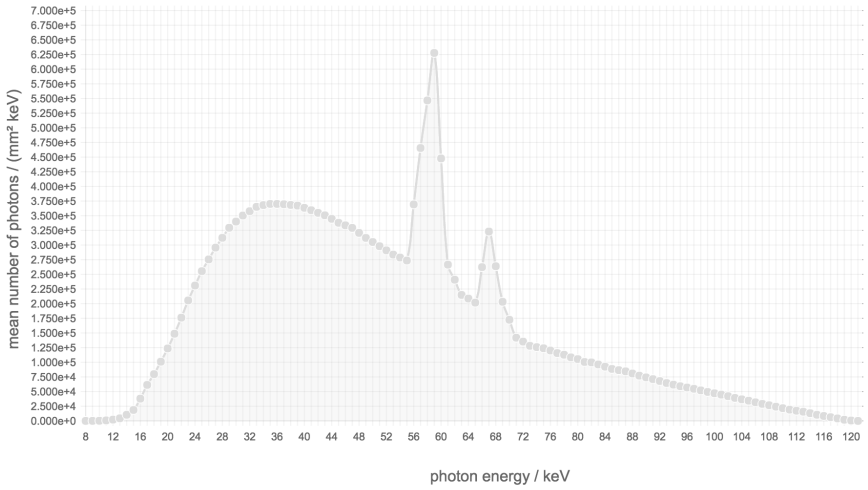

Figure 7.9: X-ray photon spectra of 120 kVp generated by Siemens tool [88].

As illustrated in Figure 7.9, the mean energy of a photon for a tube voltage of 120 kVp is approximately 60 keV. Therefore, the energy found through MC simulations that optimises the SDNR is coherent with the results reported in the literature.

7.3.1 Case Study 1: Calcification size study

In order to show another potential application of the voxelization of the phantom used in this study, also imaging calculations were performed. In particular, in

this case, the optimal X-ray energies that maximise the SDNR were determined for calcifications with different radius (0.3 cm, 0.7 cm and 1.5 cm) through MC simulations. Figure 7.10 illustrates the geometry of the different lung calcifications in the voxel phantom created. The 2D projections were reconstructed for an exposure to a monochromatic X-ray beam of 60 keV.

The results of SDNR for different calcifications sizes and for different energies are showed in Figure 7.11. For each calcification size, the lung dose was normalised to 5mGy, and the ROIs used to calculate SDNR were kept constant for the different energies and calcifications.

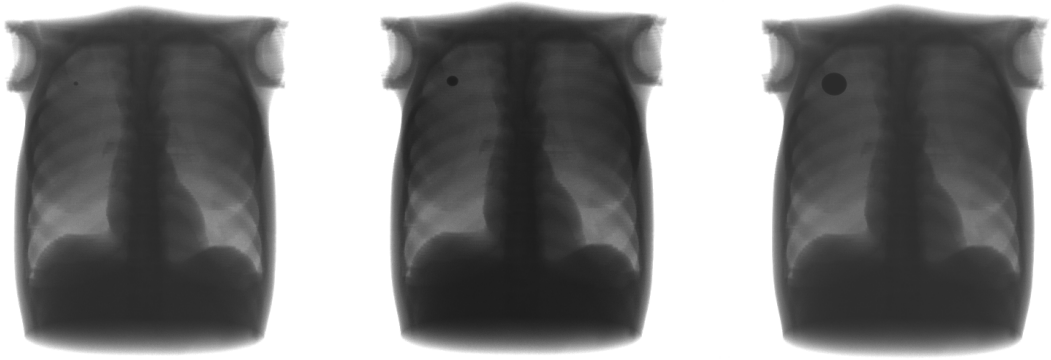

(a) (b) (c)

Figure 7.10: 2D projections of the voxel phantom with calcifications of different radius: (a) 0.3 cm, (b) 0.7 cm, (c) 1.5 cm.

As discussed in previous chapters, the attenuation of the X-ray intensities and consequently, the ability to differentiate tissues, depends on the energy of incident photons, and on the thickness of the tissue. For similar incident energies, the attenuation increases as the thickness of the tissue increases [100]. Therefore, for the same X-ray beam energy, SDNR should be greater for larger calcifications, which is demonstrated by the SDNR curves in Figure 7.11. For X-ray beams of 60 keV, the SDNR is higher for calcifications with diameters of 1.5 cm, than for 0.7 cm and 0.3 cm, 11.46, 9.94 and 3.08, respectively.

Likewise, and according to the literature [100], the optimal energy for detection of calcifications should increase with increase of calcifications sizes.

Regarding the results in Figure 7.11, is concluded that for smaller size of calcifications ($d = 3mm$) the optimal mean energy is around 40 keV, while for bigger sizes of calcifications ($d = 15mm$) the optimal energy increases to 70 keV.

Beutel [100], reported a decrease in contrast for a 0.3 cm nodule from 90 kVp to 120 kVp, which corresponds to an approximately mean energy of 53 keV and 60 keV and is congruent with the results achieved. However, besides the SDNR may

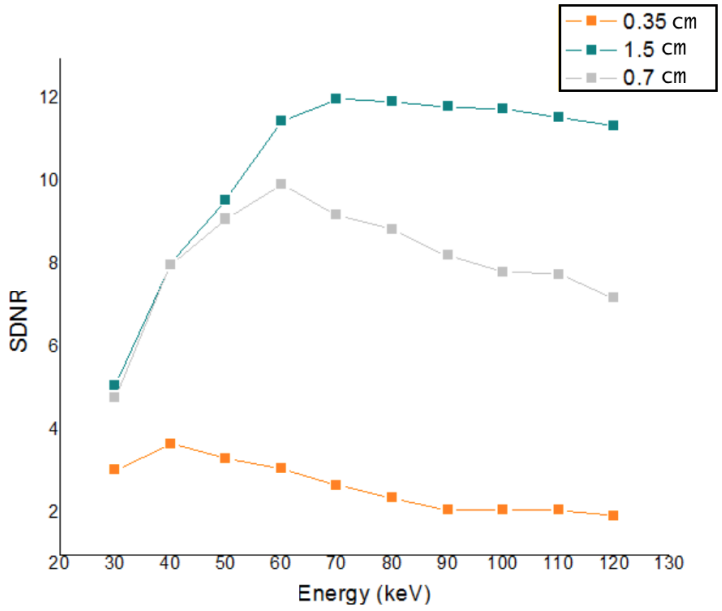

Figure 7.11: SDNR results obtained by MC simulations for different sizes of lung calcifications.

not be optimal at 120 kVp, this is the tube peak voltage chosen for lung imaging due to the higher penetration of the mediastinum and the reduced contrast of ribs, which supports the result achieved in the previous section.

Chapter 8

Conclusions

The aim of this dissertation was to implement a computational voxel phantom starting by a physical one for precise organs dose assessment in the field of X-ray diagnostic and imaging optimisation studies. In order to accomplish this task, a multidisciplinary approach involving imaging processing and MC simulations was followed.

Since the performance of computational phantoms for assessment of organs doses relies on the accuracy of organs segmentation and phantom definition, efforts were made to propose a fast, easy and accurate method for extraction of radiosensitive organs.

Initially, different thresholds were implemented in order to define body outline and to extract bones segments and air equivalent tissues. The mean values of accuracy, 0.9943 and 0.9756, and FPR, 0.0050 and 0.0308, achieved, respectively, for bone and lung segmentation, demonstrate a good agreement between the manual and the automatic segmentation and a successful definition of thresholds values.

On the other side, to segment the remaining radiosensitive organs, region growing algorithm has proven to be the best approach. In order to implement region growing algorithm, was necessary to define different initial seed points and tolerance levels for each organ. Despite an overall accuracy higher than 95 % for the different organs, Jaccard index obtained for kidney, venae cava and trachea reveal some uncertainties on segmentation. The difficulties on segmentation of these organs are due to the similarity the HU values of the kidney, venae cava and trachea in comparison with the HU values of adjacent organs as spleen, liver and lungs, respectively.

The first part of this study is important to demonstrate that a combination between application of different thresholds and region growing algorithms provides accurate results for thorax organs segmentation. However, it is important to remark that the method applied was optimised for medical images of a specific anthropomorphic phantom, Kyoto PBU-60, thus, the initial conditions as initial seed points pre-defined for the region growing algorithm may differ for another set of medical image.

During phantom definition, each voxel assigned with a label is associated to a density value. Density was determined from the average CT number of each organ using a calibration curve. The values calculated were compared to values established for an adult reference phantom. The relative differences between the tabulated and the experimental results were smaller than 10% for 9 out of the 11 segmented organs, which supports the segmentation results and the calibration curve used. The values determined were accepted as organs densities, except for trachea and lung due to high relative difference 77.914 % and 55.166 %, respectively achieved. The representation on CT images of lung, trachea and bronchus does not express the anatomic composition of the organs, i.e., the radiological anatomic, mainly air, does not reveals the constituents of lung (pulmonary tissue) and of trachea (cartilage) which influence organ density. Since density has a great influence on dose calculations, the density of both organs was adjusted to the reference values.

Due to the lack of information provided about the organs masses of the Kyoto PBU-60, the mass of the segmented organs, calculated from the product between density and volume, was also compared to reference values. Besides some significant differences between the masses determined and the references one (liver (25.45 %), trachea (-41.82 %) and breast (-15.14 %)), justified by difficulties in segmentation, the organs masses determined for the computational voxel phantom were accepted as correct.

On the second part of this dissertation, PENELOPE code was used to perform MC simulations in order to validate the voxel phantom. Firstly, MC simulations were performed to validate the implemented MC model of a CT scanner image acquisition system (Siemens SOMATOM Definition).

The MC implemented model was validated by comparing simulated results against measured results of $CTDI_{100}$ and $CTDI_w$. The final discrepancy achieved for $CTDI_w$ was 0.870%, for this reason, considering the uncertainties associated with the simulations (i.e. 15 % for input X-ray spectra data), the MC model was considered validated.

Aiming to validate the voxel phantom developed for assessment of organ doses,

the simulated result of $CTDI_{100}$ for simulations using the voxel phantom were compared against experimental $CTDI_{100}$ results. A maximum difference of 13.813 % was achieved, which considering simulation uncertainties aforementioned, validates the phantom developed in this work.

In the last part of this work, in order to show another possible application of the developed voxel phantom, the optimisation of the image quality for difference calcifications sizes has been studied. Firstly, 60 keV was found to be the optimal X-ray energy that maximises the SDNR for a calcification of 0.7 cm radius. This result is in agreement with the mean energy of an X-ray spectra of 120 kVp, the tube peak voltage normally used in lung imaging [31].

On the other side, different calcifications sizes, 0.3, 0.7 and 1.5 cm, were tested in order to evaluate the behaviour of SDNR, an increase on the SDNR with calcification size, for the some incident energy, was observed and is supported by previous studies [100]. Furthermore, it was observed an increase of the optimal energy with the increase of the calcification thickness. In fact, the optimal energy increases 75 % , from 40 keV to 70 keV, for an increase in size from 0.3 cm to 1.5 cm, respectively.

The aforementioned results support the utilisation of the voxel phantom as powerful methods for organ dose assessment and image quality studies. The voxelization of this type of physical phantom has the advantage that simulated values could be compared with measurements in Hospitals, giving more reliable results for each clinical task.

8.1 Future Work

The result of this work is satisfactory and the main goal was accomplished since the voxel phantom created was validated to use in hospital environment. However different tasks can be performed to support phantom validation and the work done.

The segmentation approach can be improved in order to distinguish bronchus from trachea and the different bones present in thorax such as ribs and spine canal. Furthermore, efforts can be made to automate the method by testing ATLAS techniques.

Regarding the voxel phantom, simulations can be performed to evaluate attenuation dose within the phantom by measuring the entrance and exit surface dose using patient skin dosimeters.

CT protocols, using different kVp and mAs, can be tested to estimate organ doses on the phantom.

Bibliography

[1] L. A. Dewerd and M. Kissick, *Phantoms of medical and health physics*. Springer-Verlag New York, 2016.

[2] X. G. Xu, "An exponential growth of computational phantom research in radiation protection, imaging, and radiotherapy: a review of the fifty-year history," *Physics in Medicine and Biology*, vol. 59, no. 18, 2014.

[3] E. A. Blakely, "Biological Effects of Cosmic Radiation: Deterministic and Stochastic," *Health Physics*, vol. 79, no. 5, p. 495–506, 2000.

[4] *Radiation protection: 1990 recommendations of the International Commission on Radiological Protection ; adopted by the commission in November 1990*. Published for the International Commission on Radiological Protection by Pergamon Press, 1992.

[5] L. Choonsik and L. Jaiki, "Computational anthropomorphic phantoms for radiation protection dosimetry: evolution and prospects," *Nuclear Engineering and Technology*, vol. 38, no. 26, 2006.

[6] R. Cierniak, *X-ray computed tomography in biomedical engineering*. Springer Science & Business Media, 2011.

[7] C. for Devices and R. Health, "Medical x-ray imaging - computed tomography (ct)." Available at: `https://www.fda.gov/radiation-emittingproducts/radiationemittingproductsandprocedures/medicalimaging/medicalx-rays/ucm115317.htm#1`.

[8] J. Santos, S. Foley, G. Paulo, M. F. McEntee, and L. Rainford, "The establishment of computed tomography diagnostic reference levels in portugal," *Radiation protection dosimetry*, vol. 158, no. 3, pp. 307–317, 2013.

[9] "Healthcare resource statistics - technical resources and medical technology," *Eurostat - Statistic Explained*, Nov 2016. Available at: `http://ec.europa.eu/eurostat/statistics-explained/index.php/Healthcare_resource_statistics_-_technical_resources_and_medical_technology`.

[10] L. Bacchus, R. D. Shah, J. H. Chung, T. P. Crabtree, D. E. Heitkamp, M. D.

Iannettoni, G. B. Johnson, C. Jokerst, B. L. McComb, A. G. Saleh, *et al.*, "Acr appropriateness criteria® occupational lung diseases," *Journal of thoracic imaging*, vol. 31, no. 1, pp. W1–W3, 2016.

[11] T.-L. H. Mohammed, A. Chowdhry, G. P. Reddy, J. K. Amorosa, K. Brown, D. S. Dyer, M. E. Ginsburg, D. E. Heitkamp, J. Jeudy, J. Kirsch, *et al.*, "Acr appropriateness criteria® screening for pulmonary metastases," *Journal of thoracic imaging*, vol. 26, no. 1, pp. W1–W3, 2011.

[12] H. Kaur, N. M. Hindman, W. B. Al-Refaie, H. Arif-Tiwari, B. D. Cash, V. Chernyak, J. Farrell, J. R. Grajo, J. M. Horowitz, M. M. McNamara, *et al.*, "Acr appropriateness criteria® suspected liver metastases," *Journal of the American College of Radiology*, vol. 14, no. 5, pp. S314–S325, 2017.

[13] K. E. Dill, E. George, S. Abbara, K. Cummings, C. J. Francois, M. D. Gerhard-Herman, H. L. Gornik, M. Hanley, S. P. Kalva, J. Kirsch, *et al.*, "Acr appropriateness criteria imaging for transcatheter aortic valve replacement," *Journal of the American College of Radiology*, vol. 10, no. 12, pp. 957–965, 2013.

[14] D. J. Brenner and E. J. Hall, "Computed tomography — an increasing source of radiation exposure," *New England Journal of Medicine*, vol. 357, no. 22, pp. 2277–2284, 2007. PMID: 18046031.

[15] *Medical radiation exposure of European population*, vol. 180. Publications Office, 2015.

[16] L. YU, X. Lui, S. Leng, J. M. Kofler, J. C. Ramirez-Giraldo, M. Qu, J. Christner, J. G. Fletcher, and C. H. McCollough, "Radiation dose reduction in computed tomography: techniques and future perspective," *maging in medicine*, vol. 1, p. 65–84, Oct 2009.

[17] E. C. Lin, "Radiation risk from medical imaging," *Mayo Clinic Proceedings*, 2010.

[18] A. L. A. Neves, *Study of pediatric exposure in CT: Assessment of radiosensitivity issues*. PhD thesis, 2011.

[19] W. A. Kalender, "Dose in x-ray computed tomography," *Physics in Medicine & Biology*, vol. 59, no. 3, p. R129, 2014.

[20] M. Rosenstein, "Diagnostic reference levels for medical exposure of patients: Icrp guidance and related icru quantities," *Health physics*, vol. 95, no. 5, pp. 528–534, 2008.

[21] F. Pernicka and I. McLean, "Dosimetry in diagnostic radiology: an international code of practice," *International Atomic Energy Agency*, 2007.

[22] ICRP, "Diagnostic reference levels in medical imaging: review and additional advice.," *ICRP Supporting Guidance 2*, vol. 31, no. 4, 2001.

[23] D. W. Jones, P. Hogg, and E. Seeram, *Practical SPECT/CT in Nuclear Medicine*. Springer-Verlag, 1 ed., 2013.

[24] E. Seeram, *Computed tomography: physical principles, clinical applications, and quality control*. Elsevier, 2016.

[25] M. Prokop and M. Galanski, *Spiral and multislice computed tomography of the body*. Thieme, 2003.

[26] R. M. Rangayyan, *Biomedical image analysis*. CRC Press, 2005.

[27] R. Schmitz, "Bioengineering 508: Physical Aspects of Medical Imaging," october 2006.

[28] L. L. Geyer, U. J. Schoepf, F. G. Meinel, J. W. Nance Jr, G. Bastarrika, J. A. Leipsic, N. S. Paul, M. Rengo, A. Laghi, and C. N. De Cecco, "State of the art: iterative ct reconstruction techniques," *Radiology*, vol. 276, no. 2, pp. 339–357, 2015.

[29] A. Padole, R. D. Ali Khawaja, M. K. Kalra, and S. Singh, "Ct radiation dose and iterative reconstruction techniques," *American Journal of Roentgenology*, vol. 204, no. 4, pp. W384–W392, 2015.

[30] M. Beister, D. Kolditz, and W. A. Kalender, "Iterative reconstruction methods in x-ray ct," *Physica Medica*, vol. 28, no. 2, pp. 94 – 108, 2012.

[31] S. Baumueller, A. Winklehner, C. Karlo, R. Goetti, T. Flohr, E. W. Russi, T. Frauenfelder, and H. Alkadhi, "Low-dose ct of the lung: potential value of iterative reconstructions," *European radiology*, vol. 22, no. 12, pp. 2597–2606, 2012.

[32] C. Lin, T. Wu, C. Lin, S. Hung, C. Chiu, M.-J. Liu, M. Teng, F. Chang, W. Guo, and C. Chang, "Can iterative reconstruction improve imaging quality for lower radiation ct perfusion? initial experience," *American Journal of Neuroradiology*, vol. 34, no. 8, pp. 1516–1521, 2013.

[33] F. Tricarico, A. M. Hlavacek, U. J. Schoepf, U. Ebersberger, J. W. Nance, R. Vliegenthart, Y. J. Cho, J. R. Spears, F. Secchi, G. Savino, *et al.*, "Cardiovascular ct angiography in neonates and children: image quality and potential for radiation dose reduction with iterative image reconstruction techniques," *European radiology*, vol. 23, no. 5, pp. 1306–1315, 2013.

[34] X. Pan, E. Y. Sidky, and M. Vannier, "Why do commercial ct scanners still employ traditional, filtered back-projection for image reconstruction?," *Inverse problems*, vol. 25, no. 12, p. 123009, 2009.

[35] L. W. Goldman, "Principles of ct: multislice ct," *Journal of nuclear medicine technology*, vol. 36, no. 2, pp. 57–68, 2008.

[36] "The measurement, reporting and management of radiation dose in ct," *Medical Physics*, vol. 34, no. 6Part24, p. 2656–2672, 2007.

[37] C. H. McCollough, S. Leng, L. Yu, and J. G. Fletcher, "Dual-and multi-energy ct: principles, technical approaches, and clinical applications," *Radiology*, vol. 276, no. 3, pp. 637–653, 2015.

[38] R. K. Kaza, J. F. Platt, R. H. Cohan, E. M. Caoili, M. M. Al-Hawary, and A. Wasnik, "Dual-energy ct with single-and dual-source scanners: current applications in evaluating the genitourinary tract," *Radiographics*, vol. 32, no. 2, pp. 353–369, 2012.

[39] S. Ulzheimer and S. Kappler, "Photon-counting detectors in clinical computed tomography," january 2017. Available at: `https://health.siemens.com/ct_applications/somatomsessions/index.php/photon-counting-detectors-in-clinical-computed-tomography/`.

[40] E. B. Podgorsak, *Radiation Physics for Medical Physicians*. Springer, 2 ed., 2009.

[41] J. Pedroso de Lima, *Técnicas de diagnóstico com raios X: aspectos físicos e biofísicos*. Imprensa da Universidade de Coimbra, 2 ed., 2009.

[42] W. R. Hendee and E. R. Ritenour, *Medical Imaging Physics*. Wiley, 4 ed., 2003.

[43] F. A. Smith, *A primer in applied radiation physics*. World Scientific Publ., 2006.

[44] H. V. Alberto, "Fisica Quântica - Uma Introdução." Apontamentos de Fisica Quântica, 2014.

[45] H. D. Nagel, *Radiation exposure in computed tomography*. CTB Publications, 2002.

[46] M. J. a. Rodrigues, *Influence of Scatter Radiation on Dose Optimization and Image Quality in Digital Breast Tomosynthesis*. PhD thesis, 2016.

[47] E. D. Cakmak, N. Tuncel, and B. Sindir, "Assessment of organ dose by direct and indirect measurements for a wide bore x-ray computed tomography unit that used in radiotherapy," *International Journal of Medical Physics, Clinical Engineering and Radiation Oncology*, vol. 4, no. 02, p. 132, 2015.

[48] C. H. Mccollough, S. Leng, L. Yu, D. D. Cody, J. M. Boone, and M. F. Mcnitt-Gray, "Ct dose index and patient dose: They are not the same thing," *Radiology*, vol. 259, no. 2, p. 311–316, 2011.

[49] T. M. Griglock, L. Sinclair, A. Mench, R. Lamoureux, b. Cormack, S. Bidari, L. Rill, and M. Arreola, "Determining organ doses from ct with direct mea-

surements in postmortem subjects: Part 1—methodology and validation," *Radiology Select (RSNA)*, vol. 227, Nov 2015.

[50] "ATOM Dosimetry Phantoms," *CIRS*. Available at: `http://www.cirsinc.com/file/Products/701_706/701%20706%20ATOM%20PB%20041717.pdf`.

[51] "CT Whole Body Phantom PBU-60," *CT Whole Body Phantom PBU-60*, 2015. Available at: `https://www.kyotokagaku.com/products/detail03/ph-2b.html`.

[52] T. Aoyama, S. Koyama, and C. Kawaura, "Organ dose measurement in x-ray ct and other diagnostic radiology by using novel photodiode dosimeters installed in an anthropomorphic phantom," *11th International Congress of the International Radiation Protection Association (IRPA 11)*, p. 23–28, May 2004.

[53] M. Stabin, M. A. Emmons, W. P. Segars, M. Fernald, and A. B. Brill, "Icrp-89 based adult and pediatric phantom series," *Journal of nuclear Medicine*, vol. 49, no. supplement 1, pp. 14P–14P, 2008.

[54] S. Kamdi and R. K. Krishna, "Image segmentation and region growing algorithm," *International Journal of Computer Technology and Electronics Engineering (IJCTEE)*, vol. 2, no. 1.

[55] H. Kalinic, "Atlas-based image segmentation: A survey," 2009.

[56] B. Haas, T. Coradi, M. Scholz, P. Kunz, M. Huber, U. Oppitz, L. André, V. Lengkeek, D. Huyskens, A. van Esch, and R. Reddick, "Automatic segmentation of thoracic and pelvic ct images for radiotherapy planning using implicit anatomic knowledge and organ-specific segmentation strategies," *Physics in Medicine & Biology*, vol. 53, no. 6, p. 1751, 2008.

[57] M. Sonawane and C.A.Dhawale, "A brief survey on image segmentation methods," *IJCA Proceedings on National conference on Digital Image and Signal Processing*, vol. DISP 2015, pp. 1–5, April 2015.

[58] L. R. Varshney, "Abdominal organ segmentation in ct images: A survey," p. 1–3, 2002.

[59] D. Ballard, U. Shani, and R. Schudy, "Anatomical models for medical images," *COMPSAC 79. Proceedings. Computer Software and The IEEE Computer Societys Third International Applications Conference, 1979.*

[60] K. T. Bae, M. L. Giger, C. T. Chen, and C. J. Kahn, "Automatic segmentation of liver structure in ct images," *Medical Physics*, vol. 2, no. 1, p. 71–78, 1993.

[61] N. Archip, P. J. Erard, M. Egmont-Petersen, J. M. Haefliger, and J. F. Germond, "A knowledge-based approach to automatic detection of the spinal cord in ct images," *IEEE Transactions on Medical Imaging*, vol. 21, pp. 1504–1516,

Dec 2002.

[62] S. Agatonovic-Kustrin and R. Beresford, "Basic concepts of artificial neural network (ann) modeling and its application in pharmaceutical research," *Journal of Pharmaceutical and Biomedical Analysis*, vol. 22, no. 5, p. 717–727, 2000.

[63] C.-C. Lee and P.-C. Chung, "Recognizing abdominal organs in ct images using contextual neural network and fuzzy rules," in *Proceedings of the 22nd Annual International Conference of the IEEE Engineering in Medicine and Biology Society (Cat. No.00CH37143)*, vol. 3, pp. 1745–1748 vol.3, 2000.

[64] J. Koss, F. Newman, T. Johnson, and D. Kirch, "Abdominal organ segmentation using texture transforms and a hopfield neural network," *IEEE Transactions on Medical Imaging*, vol. 18, no. 7, p. 640–648, 1999.

[65] "SOMATOM Definition AS," *Siemens*. Available at: `https://www.healthcare.siemens.pt/computed-tomography/single-source-ct/somatom-definition-as`.

[66] "Phantom for CTDI Meausrements," 2011. Available at: `http://www.quart.de/sites/default/files/2017-06/Quart-ctdi-eng.pdf`.

[67] Redakteur, "Implant types," *Implant types*. Availabe at: `http://www.polytech-health-aesthetics.com/index.php/en/products-pat/breast-implants/types-of-implants`.

[68] H. Cember and T. E. Johnson, *Introduction to health physics*. McGraw-Hill, 4 ed., 2009.

[69] "RaySafe Solo - User Manual," *RaySafe Solo - User Manual*, 2013. Available at: `http://www.raysafe.com/Products/Equipment/RaySafe%20Solo#Models`.

[70] A. Rosset, L. Spadola, and O. Ratib, "Osirix: An open-source software for navigating in multidimensional dicom images," *Journal of Digital Imaging*, vol. 17, pp. 205–216, Sep 2004.

[71] *MATLAB - The Language of Technical Computing*. MathWorks Inc., 6 ed., 1998.

[72] C. Revol-Muller, F. Peyrin, Y. Carrillon, and C. Odet, "Automated 3d region growing algorithm based on an assessment function," *Pattern Recognition Letters*, vol. 23, no. 1, pp. 137 – 150, 2002.

[73] F. C. Monteiro and A. C. Campilho, "Distance measures for image segmentation evaluation," *Numerical Analysis and Applied Mathematics ICNAAM*, vol. 1479, p. 794–797, 2012.

[74] Y. Zhang, "A survey on evaluation methods for image segmentation," *Pattern Recognition*, vol. 29, no. 8, pp. 1335 – 1346, 1996.

[75] T. Ferreira and W. Rasband, *ImageJ User Guide*. 2002.

[76] K. M. Ting, *Confusion Matrix*, pp. 209–209. Boston, MA: Springer US, 2010.

[77] M. E. Celebi, M. Teresa, and J. S. Marques, *Dermoscopy image analysis*. Taylor & Francis, 2016.

[78] A. R. Marçal and A. S. Rodrigues, "A method for multi-spectral image segmentation evaluation based on synthetic images," *Computers & Geosciences*, vol. 35, no. 8, pp. 1574 – 1581, 2009.

[79] C. Borges, *Impact of using different radiation therapy techniques in breat cancer: contralateral breast dose*. PhD thesis, 2014.

[80] H. Jiang, J. Seco, and H. Paganetti, "Effects of hounsfield number conversion on ct based proton monte carlo dose calculations," *Medical physics*, vol. 34, no. 4, pp. 1439–1449, 2007.

[81] Origin, "Origin and OriginPro." Avilable at `http://www.originlab.com/Origin`.

[82] F. Salvat, J. M. Fernández-Varea, and J. Sempau, "Penelope-2008: A code system for monte carlo simulation of electron and photon transport,"

[83] F. Salvat and J. M. Fernández-Varea, "Overview of physical interaction models for photon and electron transport used in monte carlo codes," *Metrologia*, vol. 46, no. 2, p. S112, 2009.

[84] C. Figueira, F. Becker, C. Blunck, S. DiMaria, M. Baptista, B. Esteves, G. Paulo, J. Santos, P. Teles, and P. Vaz, "Medical staff extremity dosimetry in ct fluoroscopy: an anthropomorphic hand voxel phantom study," *Physics in Medicine & Biology*, vol. 58, no. 16, p. 5433, 2013.

[85] J. Gu, B. Bednarz, P. F. Caracappa, and X. G. Xu, "The development, validation and application of a multi-detector ct (mdct) scanner model for assessing organ doses to the pregnant patient and the fetus using monte carlo simulations," *Physics in Medicine & Biology*, vol. 54, no. 9, p. 2699, 2009.

[86] G. Jarry, *Monte Carlo dose verification of a commercial CT scanner with application for patient specific dosimetry*. UCLA, 2002.

[87] ICRP, "Adult reference computational phantoms," *ICRP Publication 110*, vol. 39, no. 2, 2009.

[88] Siemens, "Simulation of x-ray spectra." Available at: `https://www.oem-xray-components.siemens.com/x-ray-spectra-simulation`.

[89] J. M. Boone, T. R. Fewell, and R. J. Jennings, "Molybdenum, rhodium, and

tungsten anode spectral models using interpolating polynomials with application to mammography," *Medical Physics - The International Journal of Medical Physics Research and Practice*, vol. 24, p. 1863–1874, Dec 1997.

[90] H. J. Brisse, J. Brenot, N. Pierrat, G. Gaboriaud, A. Savignoni, Y. D. Rycke, S. Neuenschwander, B. Aubert, and J.-C. Rosenwald, "The relevance of image quality indices for dose optimization in abdominal multi-detector row ct in children: experimental assessment with pediatric phantoms," *Physics in Medicine & Biology*, vol. 54, no. 7, p. 1871, 2009.

[91] F. Verdun, D. Racine, J. Ott, M. Tapiovaara, P. Toroi, F. Bochud, W. Veldkamp, A. Schegerer, R. Bouwman, I. H. Giron, N. Marshall, and S. Edyvean, "Image quality in ct: From physical measurements to model observers," *Physica Medica*, vol. 31, no. 8, pp. 823 – 843, 2015.

[92] D. J. Minnich and D. J. Mathisen, "Anatomy of the trachea, carina, and bronchi," *Thoracic Surgery Clinics*, vol. 17, no. 4, pp. 571 – 585, 2007. Thoracic Anatomy, Part I.

[93] J. M. Holbert, D. C. Strollo, *et al.*, "Imaging of the normal trachea.," *Journal of thoracic imaging*, vol. 10, no. 3, pp. 171–179, 1995.

[94] R. Kramer, V. F. Cassola, M. E. A. Andrade, M. W. C. de Araújo, D. J. Brenner, and H. J. Khoury, "Mathematical modelling of scanner-specific bowtie filters for monte carlo ct dosimetry," *Physics in Medicine & Biology*, vol. 62, no. 3, p. 781, 2017.

[95] G. Zhang, N. Marshall, R. Jacobs, Q. Liu, and H. Bosmans, "Bowtie filtration for dedicated cone beam ct of the head and neck: a simulation study," *The British journal of radiology*, vol. 86, no. 1028, p. 20130002, 2013.

[96] K. Ono, T. Hiraoka, A. Ono, E. Komatsu, T. Shigenaga, H. Takaki, T. Maeda, H. Ogusu, S. Yoshida, K. Fukushima, *et al.*, "Low-dose ct scan screening for lung cancer: comparison of images and radiation doses between low-dose ct and follow-up standard diagnostic ct," *SpringerPlus*, vol. 2, no. 1, p. 393, 2013.

[97] T. Kubo, Y. Ohno, D. Takenaka, M. Nishino, S. Gautam, K. Sugimura, H. U. Kauczor, and H. Hatabu, "Standard-dose vs. low-dose ct protocols in the evaluation of localized lung lesions: Capability for lesion characterization—ilead study," *European Journal of Radiology Open*, vol. 3, pp. 67 – 73, 2016.

[98] "CTisus - Siemens SOMATOM Sensation 64 - CT Protocols." `http://www.ctisus.com/redesign/protocols/siemens?sensation-64#`. Accessed: 2010-09-30.

[99] E. L. Nickoloff and H. L. Berman, "Factors affecting x-ray spectra.," *Radiographics*, vol. 13, no. 6, pp. 1337–1348, 1993.

[100] J. Beutel, H. L. Kundel, and R. L. Van Metter, *Handbook of medical imaging: Physics and psychophysics*, vol. 1. Spie Press, 2000.

Appendices

Chapter A

Appendix I

A.1 Segmentation Results

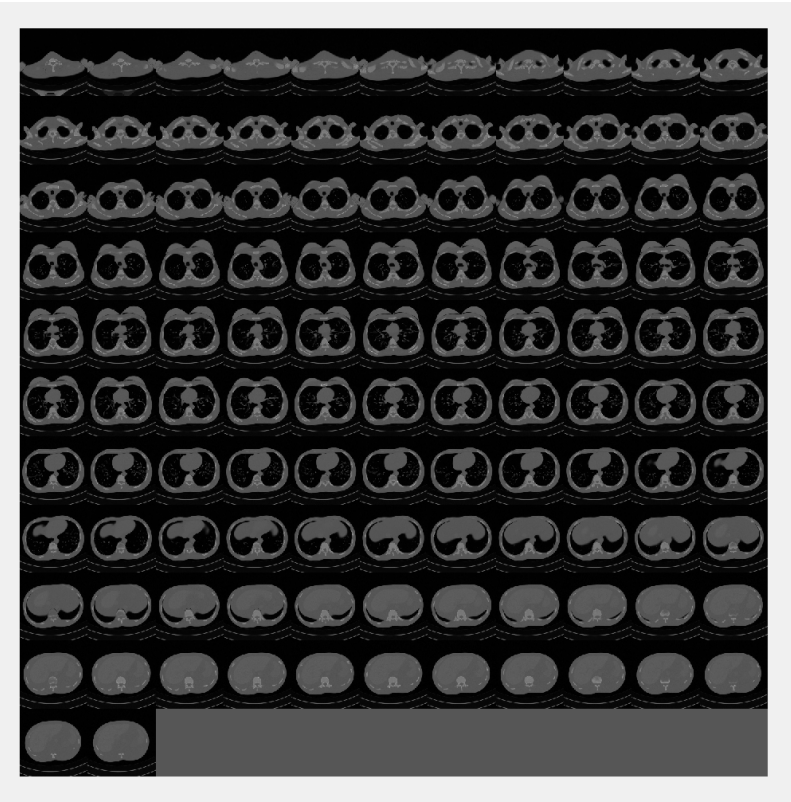

Figure A.1: Montage of the original slices.

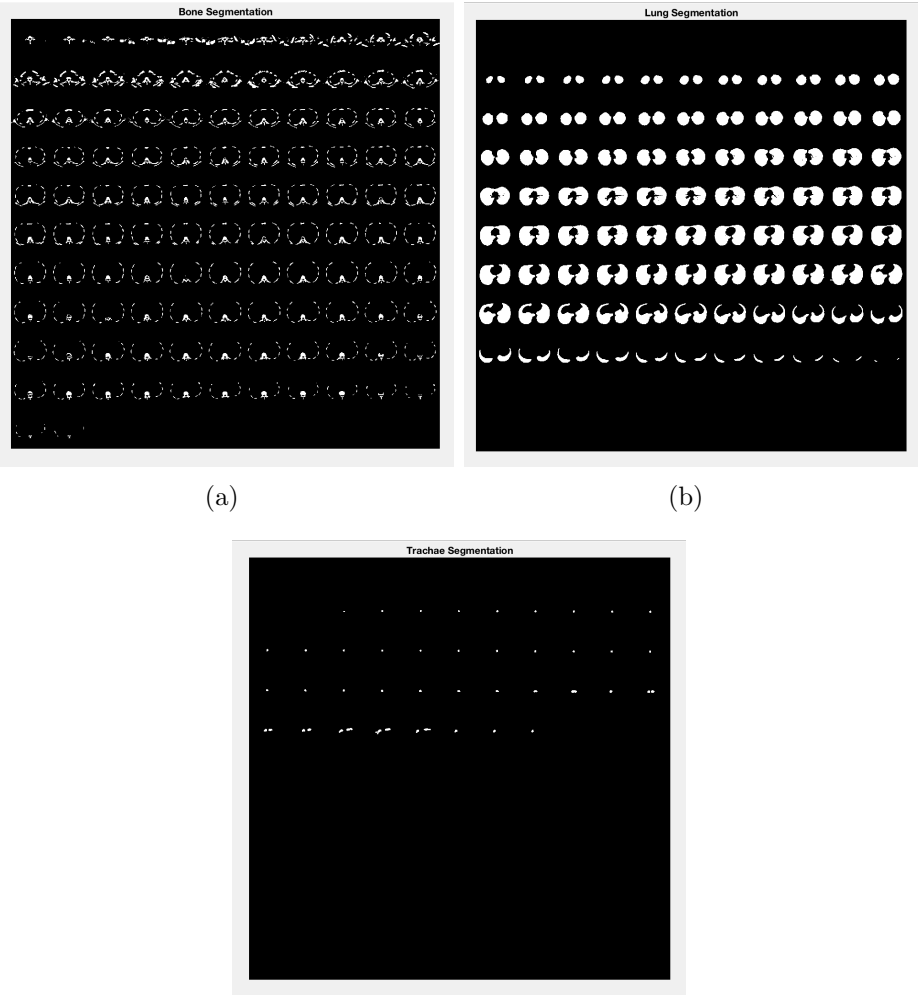

(a) (b)

(c)

Figure A.2: Montage results of thresholding methods segmentation. (a) Bone Segementation. (b) Lung Segmentation. (c) Trachea Segmentation

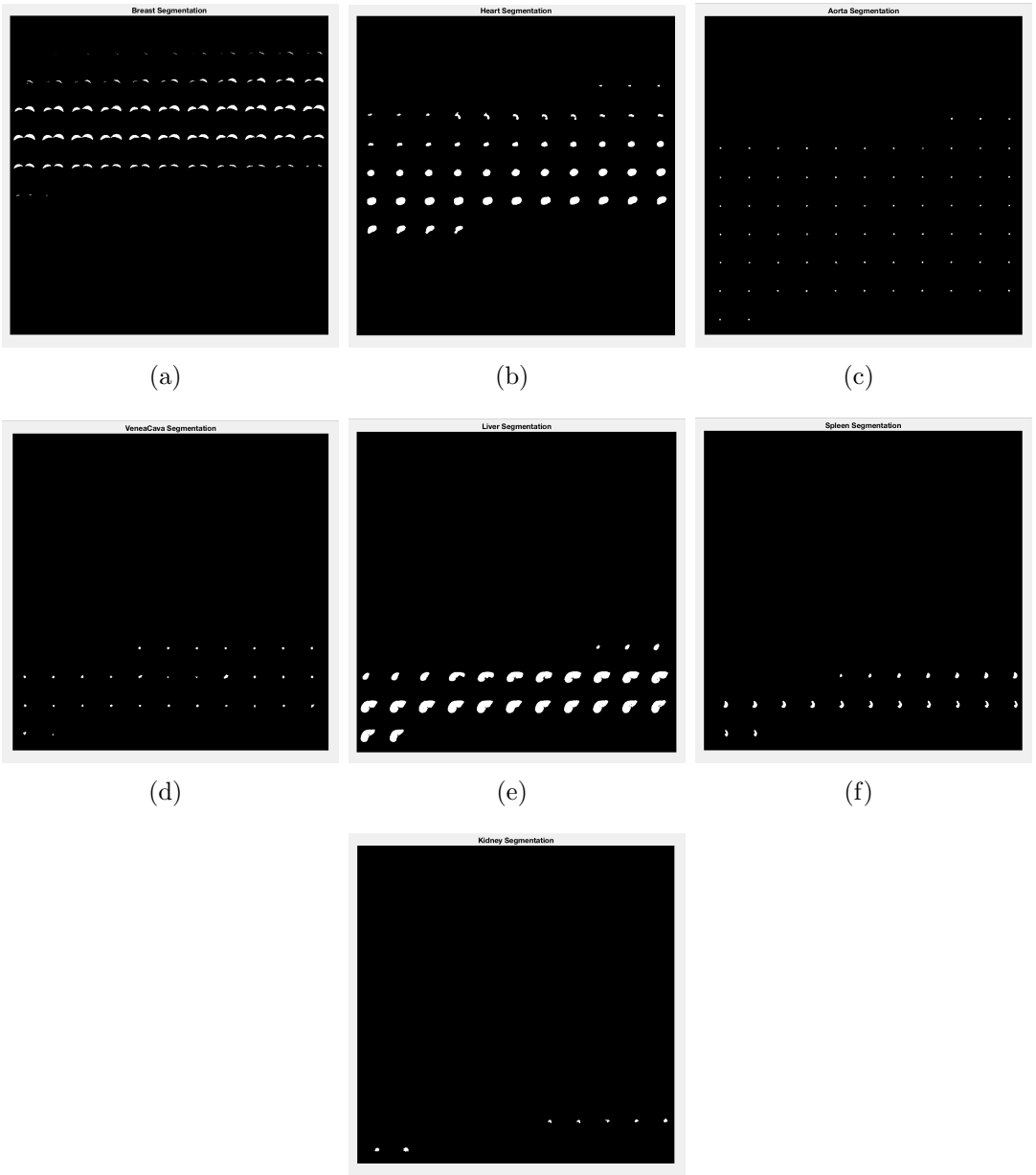

Figure A.3: Montage results of segmenattion using region growing algorithms. (a) Breast Segmentation. (b) Heart Segementation. (c) Aorta Segmentation. (d) Venae Cava Segmentation. (e) Liver Segmentation. (f) Spleen Segmentation. (g) Kidney Segmentation.

Chapter B

Appendix II

B.1 Phantom Definition

B.1.1 Material's Composition

Table B.1: List of elemental compositions (percentage by mass) for the adult female reference computational phantom. Addapted from [87]

Organ	H_1	C_6	N_7	O_8	Na_{11}	P_{15}	S_{16}	Cl_{17}	K_{19}	Ca_{20}	Fe_{20}
Bone	9.7	38.1	2.8	44.5	0.1	1.4	0.2	0.2	0.1	2.8	0.1
Liver	10.2	13.1	3.1	72.4	0.2	0.2	0.3	0.2	0.3	-	-
Heart	10.4	13.8	2.9	77.9	0.1	0.2	0.2	0.2	0.3	-	-
Kidneys	10.3	12.5	3.1	73.0	0.2	0.2	0.2	0.2	0.2	0.1	-
Spleen	10.3	11.2	3.2	74.3	0.1	0.2	0.2	0.2	0.3	-	-
Breast	11.4	46.1	0.5	42.0	-	-	-	-	-	-	-
Lung	10.3	10.7	3.2	74.6	0.2	0.2	0.3	0.3	0.2	-	-
Trachae	10.5	23.5	2.8	62.2	0.1	0.2	0.3	0.2	0.2	-	-
Air	-	-	80.0	20.0	-	-	-	-	-	-	-
SZ-50	8.41	72.25	4.61	14.73	-	-	–	-	-	-	-
Aorta Venae_Cava	10.2	11.1	3.3	74.5	0.1	0.1	0.2	0.3	0.2	-	0.1